Journal of Sound and Vibration 326 (2009) 574–598

Contents lists available at ScienceDirect

Journal of Sound and Vibration

journal homepage: www.elsevier.com/locate/jsvi

The Entropy Wave Generator (EWG): A reference case on entropy noise

Friedrich Bake [a,*], Christoph Richter [b], Bernd Mühlbauer [c], Nancy Kings [a], Ingo Röhle [a], Frank Thiele [b], Berthold Noll [c]

[a] Institute of Propulsion Technology, German Aerospace Center (DLR), Berlin, Germany
[b] Institute of Fluid Mechanics and Engineering Acoustics, Technische Universität, Berlin, Germany
[c] Institute of Combustion Technology, German Aerospace Center (DLR), Stuttgart, Germany

ARTICLE INFO

Article history:
Received 19 December 2008
Received in revised form
22 April 2009
Accepted 13 May 2009
Handling Editor: C.L. Morfey
Available online 13 June 2009

ABSTRACT

The entropy noise mechanism was investigated both experimentally and numerically on a generic test case. The model experiment features electrical heating to generate non-isentropic perturbations in a spatially varying average flow field. This flow field is set by the geometrical boundary conditions of an axisymmetric convergent–divergent nozzle in an otherwise straight tube. The considered flow conditions range from low subsonic to a transonic chocked base flow. The general response of the system to an abrupt heating pulse is studied experimentally and numerically. Furthermore, for two specific cases a detailed investigation of the pressure response in the outlet section is provided. Comprehensive experimental data are provided for the validation of numerical methods with respect to entropy noise. The numerical investigations use a commercial available computational fluid dynamics (CFD) method with partially and non-reflective boundary conditions for unsteady compressible simulations on one hand and a high-order CAA method with a time-domain impedance model on the other hand. It is found that the determination of reflections from the downstream and/or upstream open ends of the test configuration are necessary for the correct prediction of the experiment. The results of both methods are analyzed for the presence of acoustic sources considering the source term of an acoustic analogy and the acoustic intensity, respectively. Strong sources are found in the convergent/divergent nozzle by both methods. These sources show a much larger source strength than the direct sources due to the unsteady heat input. A saturation of the peak pressure response with a increasing Mach number in the nozzle throat above 0.8 is attributed to a phase shift of the source contributions between nozzle and diffuser.

The presented results enable a deep understanding of the entropy noise phenomenon especially due to the combination of experiments and two fairly different numerical approaches. However, even in spite of the simplified model case the investigated entropy noise mechanism still appears in a comprehensive complexity. Therefore, and because of the increasing relevance as an aero-engine noise source, further research on entropy noise, also under application of the presented reference cases, should be performed.

* Corresponding author.
E-mail address: Friedrich.Bake@DLR.de (F. Bake).

0022-460X/$ - see front matter © 2009 Elsevier Ltd. All rights reserved.
doi:10.1016/j.jsv.2009.05.018

Nomenclature

A	downstream propagating acoustic wave
B	upstream propagating acoustic wave
c	speed of sound
c_p	specific heat capacity
e	specific energy per volume
h	specific enthalpy
$\mathbf{I}$	intensity vector
I	intensity component
K	relaxation coefficient
L	length
m	face reactance (EHR)
Ma	Mach number
n	index
p	pressure
P	power (energy per time)
$\dot{q}$	heat input per vol. and time
q	source term
q_s	acoustic source strength
Q_V	volume integral of the source term
r	reflection coefficient
R	acoustic resistance
R_{EHR}	face resistance (EHR)
S	surface
t	time
T	temperature
T_l	period time (EHR)
$\mathbf{u}$	velocity vector
u	velocity
V	volume
x	cartesian coordinate
X	acoustic reactance
Y	mass fraction
Z	impedance
Z_0	characteristic impedance
Z_{ml}	termination impedance
$Z_{ml,\mathrm{n}}$	normalized termination impedance
$\langle\cdot\rangle_t$	time average
α	volumetric expansion coefficient
β	cavity reactance (EHR)
γ	ratio of the specific heats
ε	cavity resistance (EHR)
ϱ	density
ϱ_e	excess density
σ	coupling parameter
τ_{ij}	shear stress tensor
ϕ	acoustic potential
ψ	stream function
ω	angular frequency
$'$	small perturbation
0	mean flow state
a	acoustic perturbation
x	axial component

1. Introduction

Entropy noise is generated by the interaction of a fluid flow with a non-isentropic perturbation from the mean state. The potential impact of such a source mechanism which uses energy from large non-isentropic perturbations e.g. from a technical combustion process and a high energetic transonic flow to generate noise is obvious. The mechanism has a possible impact in many fields and technical applications. However, the experimental and theoretical quantification is insufficient with respect to the real contribution of the mechanism to the sound field in the specific application. Thus, the current paper investigates one of the indirect source mechanisms for the generation of noise in combustor flow systems on a basic physical level. The investigation is carried out experimentally and numerically.

In a combustion system the noise generated directly by the unsteady combustion process is called direct combustion noise while indirect combustion noise describes the noise contribution by accelerated flow perturbations like entropy or vorticity fluctuations.

The understanding of unsteady fluid flow phenomena in a medium at rest as a superposition of different physical modes of perturbation probably goes back to the beginning of modern research in fluid dynamics. The modes are characterized by their physical properties as entropy, vorticity and acoustic mode of perturbation. Later Chu and Kovasznay [1] analyzed the interaction of these modes. They found that in a medium at rest in average, the interaction would be a second-order effect [1]. The entropy mode, which is silent in a constant flow may transfer energy to acoustic and vorticity mode and vice versa by a nonlinear interaction. Furthermore, when considering a technical flow system for energy conversion from hot or cold gases, the average flow would vary spatially in the order of the mean state of pressure and density. The transonic flow in the combustor and the exit usually leads to velocity variations in the range of the speed of sound. Then, the analysis of Chu and Kovasznay [1] provides the qualitative statement that the interaction of the leading order mean flow variation with a first-order perturbation leads to a first-order interaction effect. However, such a variation of the base flow is not explicitly considered in this early theory.

Thus, a publication of Morfey [2] can be considered as one of the first analytical investigations of noise generation by accelerated or decelerated entropy waves. This work was an extension of the Lighthill theory [3] on jet noise by the so-called "excess jet noise" caused by density inhomogeneities in a free jet, e.g. of aero-engines. Following an analytical estimation by Morfey the excess jet noise scales with the sixth power of the jet velocity. Howe [4] picked this extended Lighthill analogy up and formulated the noise generation in inhomogeneous and non-isentropic flows with an acoustic wave operator (see [4, equation 4.14]).

Ffowcs Williams and Howe [5] developed an analytical solution for the sound generation of sharp-fronted or spherical pellet-like entropy fluctuations in a nozzle flow. Applying the Green function Ffowcs Williams and Howe formulated the sound propagation of entropy noise in an adjacent duct as well as under free field conditions. However, these solutions were limited to low Mach number flows. Also for low Mach number flows Lu [6] developed a one-dimensional analytical model for the prediction of entropy noise based on correlation quantities of temperature, pressure and velocity fluctuations.

The noise generation by entropy waves in nozzle and diffuser flows at higher Mach numbers was described by Marble and Candel [7] for compact elements in a one-dimensional theory. Here, the length of the nozzle or diffuser, respectively, have to be small in comparison to the regarded wave length (entropy or acoustic wave) in order to fulfil the compactness assumption.

Cumpsty and Marble [8,9] refined and applied this one-dimensional theory on an unreeled turbine stage. In a quasi-two-dimensional (axial and azimuthal) system the turbine stage was modeled as an in axial direction infinite thin discontinuity plane where the static pressure as well as the amplitude and direction of the flow velocity is changed. One result of these investigations was a strong increase of entropy noise generation with an increase of the pressure drop over a turbine stage. Furthermore, Cumpsty [10] described the generation of pressure, vorticity and entropy waves in a flow with fluctuating heat release. That allowed to compare the amplitude of directly generated noise to the one of entropy noise in a simplified turbine stage. As a result of this analytic estimation was the indirect entropy noise dominating the direct combustion noise. First comparisons of the total sound power of several aero-engines showed a good agreement to the results of this prediction method especially for operating conditions with low jet noise contribution [8].

In general, the interaction of turbulence and combustion is identified by Strahle in a review article [11] as the main source of sound generation in combustion systems. The contribution of entropy noise to the total noise emission was not known at this stage mainly due to the lack of experimental work in this field.

In the seventies also the first numerical approaches concerning entropy noise arose. Mathews [12] compared on behalf of the Federal Aviation Administration, U.S. Department of Transportation, different prediction tools for combustion noise in aero-engines. Following this study for turbojet engines of the manufacturer Pratt and Whitney the direct combustion noise was dominating the entropy noise. Using the method of characteristics Bloy [13] calculated numerically the pressure pulses produced by accelerated entropy waves. Referring to combustion test rigs with open outlet conditions, i.e. without acceleration in the combustor outlet, Strahle and Muthukrishnan [14] developed in a numerical–empirical way a correlation for the total combustion sound power. However, due to the restriction to open combustion chamber outlet conditions the indirect noise phenomena have been neglected. Direct numerical simulations of turbulent combustion flows by Tanahashi et al. [15] resolved the sound generated by accelerated entropy waves as the main contribution to the total noise radiation.

In the field of experimental entropy noise research only little work was published yet like Strahle [11] already mentioned. At the California Institute of Technology (Caltech) a similar test rig like the Entropy Wave Generator (EWG) test rig presented in this paper was investigated [16–18]. But in these experiments the amplitude of the induced temperature fluctuation was with approx. 1 K very low. Furthermore, due to technical restrictions at this time a post-processing of the acquired data in the time domain was not possible.

By the means of coherence analysis of different sensor signals from the inside and the outside of the combustion chamber Muthukrishnan et al. [19] determined the separation of the different combustion noises sources on a test rig for aero-engine combustors. The results showed a dominating broadband entropy noise contribution to the total noise spectrum. Similar experiments are described by Guedel and Farrando [20] on a helicopter engine from the manufacturer Turbomeca. Guedel identifies using a three-signal coherence technique a mainly low frequency sound source domain located between combustion chamber and low pressure turbine. Recently, microphone-array measurements of a GE aero-engine for regional aircraft (CF34-10E) in an open air test bed have been published by Martinez [21]. Comparing different acoustic damping materials for the hot stream liner a significant part of the total noise emission related to combustion noise was detected. However, the allocation of this noise origin to direct or indirect combustion noise generation mechanisms could not be determined.

Within the framework of the SILENCE(R) EU project Harper-Bourne et al. [22] analyzed core combustor noise during in-cell noise tests on the ANTLE engine using cross-correlations between rumble probe and microphone signals. It was found that the direct combustion noise was dominant at low frequencies below 100 Hz while the entropy noise peaks at 200 Hz and appears to dominate the combustor noise at high frequencies.

During the last 20 years a lot of research was conducted in order to reveal the role of entropy waves and entropy noise with respect to the feedback mechanisms of thermoacoustic instabilities. In this context Keller et al. [23] found in a linear stability analysis that entropy noise can be one of the possible feedback mechanisms. But Keller [24] also showed that the entropy noise phenomenon does not cover the entire instability region for combustion oscillations. Similarly Dowling [25–27] formulated indirect combustion noise as one source term in an acoustic energy equation for combustion systems.

With respect to combustion oscillations Polifke et al. [28] presented analytically the possibly constructive or destructive interference of direct combustion noise and entropy noise. But following Sattelmayer [29] the indirect combustion noise has no noticeable destabilizing effect on the stability of a simplified combustor model due to the high dispersion rate of the convecting entropy waves. In a mathematical approach Ali and Hunter [30] formulated on the other hand a possible resonant interaction between sound waves and quasi-spatially fixed entropy waves.

A numerical study by Dowling [31] did explicitly exclude the entropy noise mechanism since the oscillation behavior of configurations only with open combustion chamber outlets have been taken into account. Zhu et al. [32] specified as a result of a flow simulation (computational fluid dynamics, CFD) of a choked combustion chamber outlet system with a subsequent stability analysis entropy noise as the dominant feedback mechanism for the combustion instability of the regarded configuration.

Experimental research to evaluate the importance of entropy noise on combustion oscillations was conducted by Eckstein [33,34] by the variation of the outlet condition (open and choked nozzle) on a combustor test rig. The investigation showed on the one hand that combustion oscillation can be also very strong in the absence of entropy noise (configuration with an open combustion chamber outlet) but on the other hand in case of the choked outlet nozzle a clear contribution of entropy noise to the emitted noise spectrum exists.

Just recently the results of a numerical study by Leyko et al. [35] have been published, which predict the indirect combustion noise being one order of magnitude larger than the direct combustion noise for current aero-engines.

It can be summarized that a distinct qualitative and quantitative experimental determination of the entropy noise source mechanism was not carried out up to now and a comprehensive parameter study on entropy noise for validation purpose of numerical and analytical models is still missing. This was the motivation of the work presented here, where the complexity of the entropy noise generation process is reduced and therewith a doubtless experimental proof of entropy noise can be provided.

2. Experiment

In order to reduce the complexity of the entropy noise phenomenon prescribed above a reference test rig, the so-called Entropy Noise Generator test rig has been developed, designed and investigated. The main characteristics of this test rig are the well defined flow and boundary conditions as well as the possibility of inducing specifically controlled entropy waves and of detecting the subsequent generated entropy noise.

2.1. Experimental setup

The setup of the EWG, shown in Fig. 1, consists basically of a straight tube flow with a heating module and a nozzle where the flow is accelerated. The flow, supplied by the laboratory compressed air system through a mass flow controller, enters the setup into a settling chamber with a honeycomb flow straightener. From the settling chamber the flow is conducted via a bell mouth intake into the first tube section with a length of ≈ 250 mm and a diameter of 30 mm.

In the middle of this tube section the heating module is located. It is composed of six rings each of them with 10 heating wires stretched over the cross section. The wires made of platinum have a diameter of 25 μm and sum up over the six rings to an effective wire length of ≈ 1260 mm. Using a custom-built electronic delay circuit it is possible to heat electrically the six wire rings at the same time or to operate the six rings delayed corresponding to the convection time of the flow. Therewith, different edge shapes of the induced entropy waves can be produced.

After the heating module the flow is strongly accelerated through a convergent–divergent nozzle structure. Depending on the mass flux the Mach number in the nozzle throat (diameter = 7.5 mm) can be adjusted up to $Ma = 1$. Adjacent to the divergent nozzle part follows another tube section with a length of ≈ 1020 mm and a diameter of 40 mm. In this tube section four microphones (G.R.A.S., type 40BP) are wall-flush mounted at different axial positions. Setting the origin of the coordinate system in the plane of the most downstream heating module ring on the center axis of the tube and with the direction of the x-axis along the tube axis in downstream direction, the microphone positions are $x_{AGR1} = 456$, $x_{AGR2} = 836$, $x_{AGR3} = 1081$ and $x_{AGR4} = 1256$ mm. According to this coordinate system the nozzle throat is located at $x_{\text{nozzle}} = 105.5$ mm.

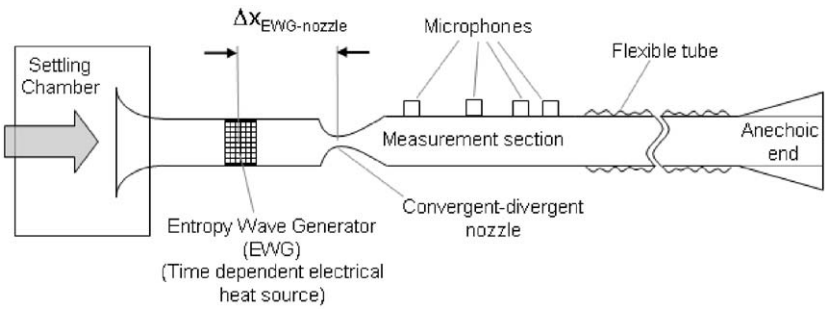

Fig. 1. Sketch of the Entropy Wave Generator (EWG) test rig; tube section $\Delta X_{\text{EWG-nozzle}}$ is variable, corresponding to different propagation lengths of entropy waves.

The microphone tube section is connected to a flexible tube of ≈ 980 mm length with the same diameter (40 mm) and an adapter section (from round to square cross section) of ≈ 280 mm. The test rig ends with a reflection minimizing termination with an inner square cross section (40 mm × 40 mm). A photo of the EWG test rig is shown in Fig. 2.

2.2. Reference test cases

The modular setup of the EWG test rig enables the investigation of the influence of a variety of different parameters on entropy noise generation.

For the comparison with numerical simulations two reference cases have been selected and documented in detail. The two cases differ in the nozzle Mach number and in the amount and control of the electrically induced heating energy. Furthermore, a different entropy wave detection and determination method was applied.

In case 1 the mass flow rate was set to 42 kg/h with a corresponding nozzle Mach number of 1.0. The entropy wave was generated by the simultaneous pulse shape heating of four heating module rings (nos. 3–6) for a pulse duration of 100 ms. This pulse excitation was repeated once per second to enable a phase averaging over 300 pulse events. The entropy wave was detected between the heating module and the nozzle at the axial position of $x = 34$ mm by a bare wire thermocouple (R-type) with a wire diameter of 1/1000 in (≈ 25 μm). The average temperature fluctuation amplitude was ≈ 9.1 K.

The mass flow rate in case 2 was set to 37 kg/h which corresponds to a subcritical nozzle Mach number of $Ma_{\mathrm{nozzle}} = 0.7$. In contrast to case 1 the rings of the heating module (nos. 1–6) were heated one after the other with a delay according to the flow velocity in the tube and the distance between each heating ring. Therefore, a certain spatial sharpness and resolution of the induced entropy wave could be achieved. In case 2 the temperature pulse was measured by applying a vibrometer and evaluating the change of the optical path length through the tube resulting from the temperature caused density change in the flow. The averaged amplitude of the temperature fluctuation in case 2 was ≈ 13.4 K.

All relevant parameters concerning the flow, the excitation and the geometric conditions of the two reference cases are listed in Table 1.

2.3. Experimental results

The results of the two reference cases are shown in the Figs. 3 and 4. The dashed red line in the upper half of the plots displays the time signal of the temperature fluctuation measured in case 1 with the fast thermocouple and in case 2 with the vibrometer (see also Table 1).

In both cases the temperature pulse with a duration of 100 ms is observable. However, the edge steepness in case 1 is decreased due to the time constant of the thermocouple, which has a cut-off frequency of only a few Hz.

The solid black line in the lower half of the figure represents the response pressure signal of the fourth microphone in the measurement tube section downstream of the nozzle. In both cases the pressure signal shows a positive pressure pulse by the time when the temperature pulse reaches the nozzle.

This pulse is followed by a certain oscillating behavior presumably due to acoustic reflections in the test setup. At the time when the trailing edge of the temperature pulse reaches the nozzle a negative pressure pulse is generated and detected by the microphones.

In order to estimate the necessary space and time resolution required for the numerical simulations, the spectral content of the acoustic pressure signals in the measurement tube was evaluated. Fig. 5 illustrates the power spectral density of the microphone signal at position x_{AGR4} for both reference cases 1 (solid line) and 2 (dashed line) and the scaled power spectral density of the heating pulse (dotted line). It is obvious that most of the energetic spectral content of the acoustic pressure signals occurs below ≈ 100 Hz.

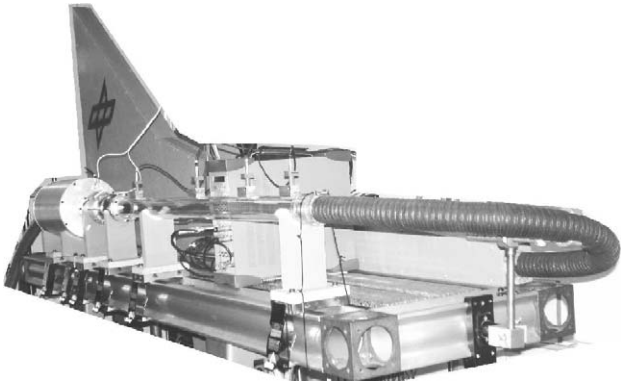

Fig. 2. Photo of the Entropy Wave Generator (EWG) test rig.

Table 1
Parameters concerning the flow, the excitation and the geometric conditions of the EWG reference test cases.

Parameter	Case 1	Case 2
Mass flow rate (kg/h)	42	37
Nozzle Mach number	1.0	0.7
Pressure (settling chamber; between honeycomb flow straightener and tube inlet; against ambient pressure) (kPa)	11.17	4.34
Pressure (nozzle; against ambient pressure) (kPa)	−52.71	−32.65
Pressure (ambient) (hPa)	1008	1013
Mean flow velocity in the tube (upstream of the nozzle; bulk velocity determined by pressure, mass flow rate and tube cross section) (m/s)	12.18	11.39
Pulse duration (ms)	100	100
Pulse repetition rate (s)	1	1
Pulse voltage (averaged over entire pulse) (V)	67.5	62.4
Pulse current (averaged over entire pulse) (A)	2.1	3.1
Heating power (electrical) (W)	143.7	192.7
Temperature increase ΔT (measured by R-type-thermocouple (1/1000 in) at $x =$ 34 mm for case 1 and by vibrometer at $x = 47.5$ mm for case 2) (K)	9.1	13.4
Heating power (determined with ΔT) (W)	106.8	138.2
Heated wire rings (no. 1 is the most upstream wire ring; no. 6 is the closest wire ring to the nozzle (also position of $x = 0$))	Nos. 3–6 simultaneously	Nos. 1–6 with delay according to flow velocity
x-position of the nozzle throat (x_{nozzle}) (mm)	105.5	105.5

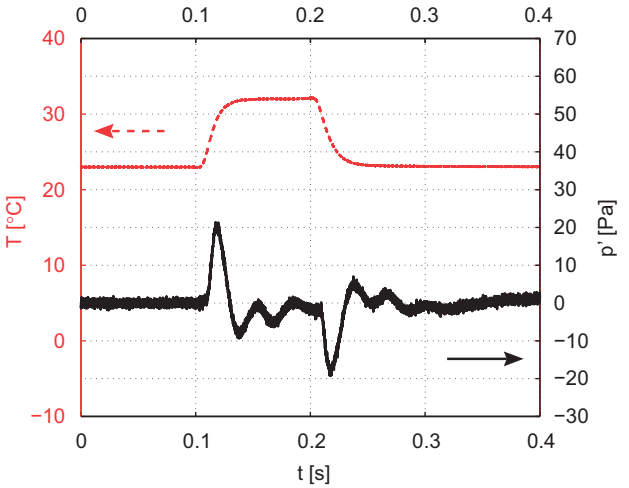

Fig. 3. Reference test case 1: flow temperature signal (dashed line, measured by thermocouple) and pressure fluctuation signal at the fourth microphone position x_{AGR4} (solid line).

Besides the reference cases in the previous section the dependency of entropy noise on different parameters has been investigated. Two of the main parameters are: on the one hand the amplitude of the accelerated temperature fluctuation and on the other hand the Mach number in the nozzle throat.

Fig. 6 shows the amplitude of the generated sound pressure pulse as a function of the amplitude of the temperature fluctuation for two different nozzle Mach numbers $Ma_{\text{nozzle}} = 0.15$ and 1. For both nozzle Mach numbers the amplitude of the generated entropy noise increases linearly with the amplitude of the temperature pulse. This confirms the expected behavior found in the literature by Marble and Candel [7].

Fig. 7 displays the amplitude of the generated sound pressure pulse as a function of the nozzle Mach number for two different amplitudes of the temperature fluctuation $\Delta T = 7.5$ and 9 K. Here, the relationship is not linear as in Fig. 6. In the nozzle Mach number regime between $Ma_{\text{nozzle}} = 0.15$ and 0.5 the pressure amplitude shows a strong increase with the Mach number. However, above a nozzle Mach number of $Ma_{\text{nozzle}} \approx 0.5$ the sound pressure amplitude saturates and even decreases slightly for higher Mach numbers up to $Ma_{\text{nozzle}} = 1$. This behavior applies to both amplitudes of the temperature fluctuation for $\Delta T = 7.5$ and 9 K, although for the temperature pulse of $\Delta T = 9$ K the entropy noise increases again slightly for the last operating point at $Ma_{\text{nozzle}} = 1$.

A combination of the two parameters temperature amplitude and nozzle Mach number is displayed in Fig. 8. Here, the entropy noise amplitude is normalized with the ambient pressure and the scaled temperature fluctuation.

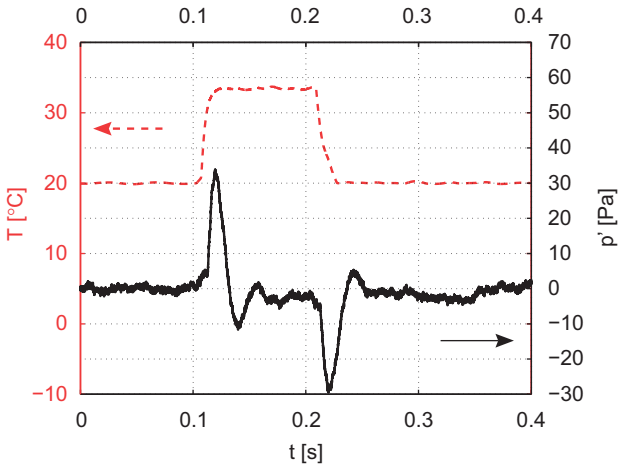

Fig. 4. Reference test case 2: flow temperature signal (dashed line, measured by vibrometer) and pressure fluctuation signal at the fourth microphone position x_{AGR4} (solid line).

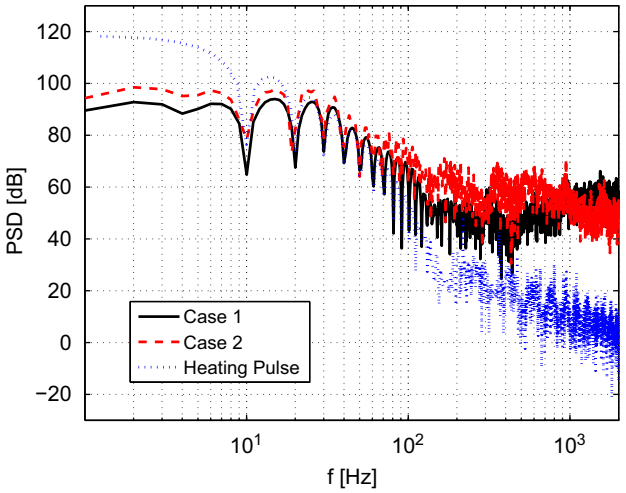

Fig. 5. Spectral content of the acoustic pressure signal at microphone position x_{AGR4} for both reference test cases 1 (solid line) and 2 (dashed line) and the heating pulse (dotted line).

For the lower Mach number region up to $Ma_{\text{nozzle}} \approx 0.5$ the normalized entropy noise increases with the nozzle Mach number proportional to a functional relation of $|\hat{p}| \sim (Ma_{\text{nozzle}})^{0.74}$. At a nozzle Mach number of $Ma_{\text{nozzle}} \approx 0.6$ the entropy noise reaches a maximum. It decreases slightly for higher Mach numbers up the choked nozzle state condition of $Ma_{\text{nozzle}} = 1$.

In order to allow an adequate numerical modeling of the test rig configuration the termination impedance at the outlet of the measurement section has been determined experimentally. Therefore, the EWG, with the flow conditions of reference case 1 (see Table 1) was excited periodically in the frequency range from 20 to 55 Hz in steps of 5 Hz and in the range from 55 to 205 in steps of 10 Hz. For each measurement point at each frequency the sound field in the measurement tube was decomposed into the downstream and upstream propagating waves. This was accomplished by applying the multi-microphone method [36,37] to the signals of the four microphones in the measurement tube. In result the decomposed acoustic wave components are evaluated to calculate the termination impedance of the setup using the following equation:

$$Z_{ml,\text{n}} = \frac{Z_{ml}}{\varrho_0 c S} = \frac{(A+B)(A-B)^*}{|A-B|^2}, \tag{1}$$

where $Z_{ml,\text{n}}$ is the normalized termination impedance and A and B are the complex acoustic waves in the frequency domain propagating in the downstream and upstream direction, respectively.

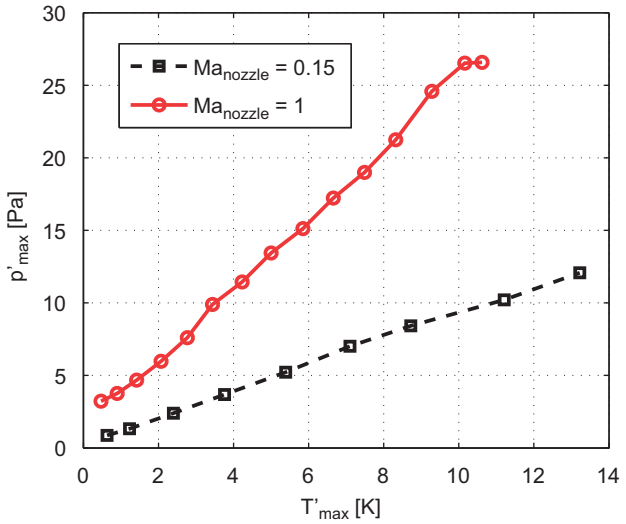

Fig. 6. Entropy noise over entropy wave amplitude: amplitude of the generated sound pressure pulse as a function of the amplitude of the temperature fluctuation for two different nozzle Mach numbers $Ma_{\text{nozzle}} = 0.15$ and 1.

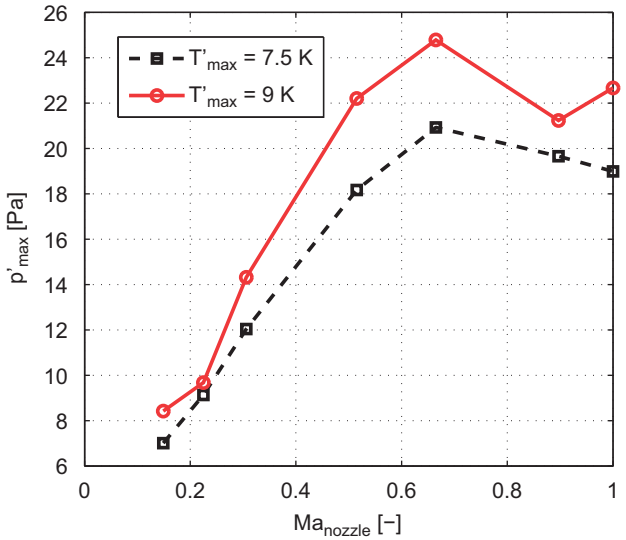

Fig. 7. Entropy noise over nozzle Mach number: amplitude of the generated sound pressure pulse as a function of the nozzle Mach number for two different amplitudes of the temperature fluctuation $\Delta T = 7.5$ and 9 K.

Fig. 9 displays the real part (dashed line) and the imaginary part of the impedance (solid line). Due to its definition this impedance is related to a reference plane or axial position. In order to avoid confusions this reference plane was set to the axial position of $x = 0$ (the plane of the most downstream heating module ring). For the implementation into numerical configurations these values have to be phase shifted to the respective outlet plane of the numerical domain. It can be assumed that the termination impedance is very similar for reference case 2, since the differences of the two reference cases in the mean flow conditions would not have a major impact on the acoustic properties of the test rig termination.

3. Numerical simulation: computational fluid dynamics

In this section, numerical simulations of the reference test case 1 and a Mach number variation applying a compressible unsteady Reynolds averaged Navier–Stokes (URANS) approach in combination with appropriate acoustic boundary conditions are presented.

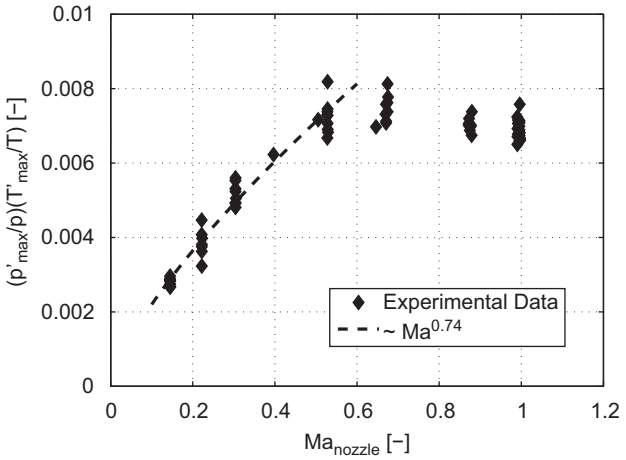

Fig. 8. Normalized entropy noise over nozzle Mach number measured at the EWG test rig.

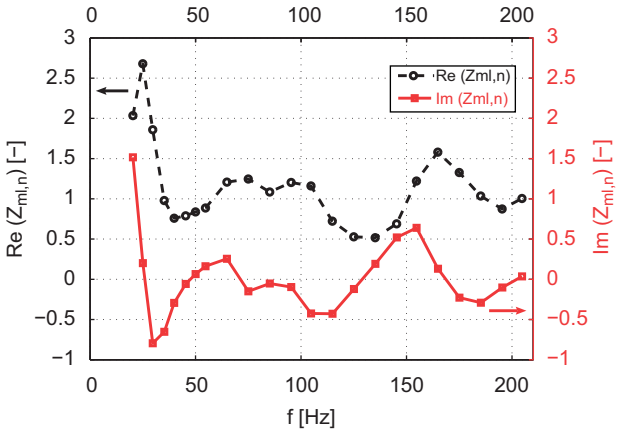

Fig. 9. Impedance of the reflection minimizing termination of the EWG test rig at reference test case flow conditions (referred to reference plane: $x = 0$, see Section 2.1).

3.1. Numerical setup

The commercial software package ANSYS CFX 11 was used to conduct the computations. The numerical simulation of the EWG can be performed in a two-dimensional framework. However, in order to meet the requirements of ANSYS CFX 11 the numerical simulations were performed on a three-dimensional unstructured grid. The rotational symmetric geometry was represented by a segment of 10°. This reduces the number of nodes to 57 000. The mesh is appropriate to adequately resolve acoustic perturbation frequencies up to $f = 2800$ Hz and hydrodynamic perturbation frequencies up to $f = 99$ Hz for the reference cases 1 and 2 in Table 1 based on a sufficient accuracy above 50 points per wavelength (PPW). For the calculations of the maximal resolved frequencies, the average speed of sound and the average axial velocity of the standard configuration downstream the heating module were considered. A outline of the computational domain is displayed in Fig. 10.

For a precise numerical simulation of acoustic phenomena like entropy noise, the acoustical behavior at the boundaries has to be taken into account appropriately. In the present case, the outlet boundary was located at the outlet of the flexible tube section of the EWG. Therefore, the boundary condition has to capture the acoustical behavior, i.e. the impedance, of the downstream geometry which is not considered by the computational domain. The experimentally determined impedance of the downstream termination is displayed in Fig. 9.

The impedance $Z(\omega)$ characterizes the properties of an acoustically reacting element in the frequency domain and is defined as the ratio of the acoustic pressure and the corresponding acoustic velocity component normal to the surface of the acoustically reactive element [38]

$$Z(\omega) = \frac{\hat{p}(\omega)}{\hat{u}_n(\omega)}, \tag{2}$$

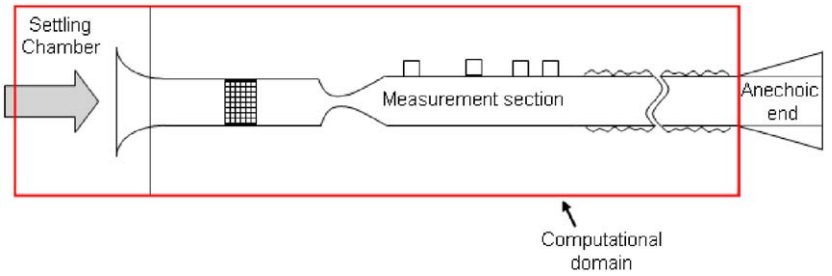

Fig. 10. Sketch of the computational domain of the Entropy Wave Generator (EWG).

where ω denotes the angular frequency and the hat the Fourier transforms. In the complex formulation of the impedance $R(\omega)$ denotes the acoustic resistance and $X(\omega)$ the acoustic reactance

$$Z(\omega) = R(\omega) + \mathrm{i}X(\omega). \tag{3}$$

The reflection factor $r(\omega)$ is the ratio of the reflected to the incident acoustic wave and is defined as

$$r(\omega) = \frac{Z(\omega) - Z_0}{Z(\omega) + Z_0}, \tag{4}$$

with the characteristic impedance of the medium Z_0

$$Z_0 = \varrho_0 c_0. \tag{5}$$

A reflection factor of $r(\omega) = 0$ corresponds to a acoustically non-reflective element and $r(\omega) = 1$ to a fully reflective element.

Due to the lack of experimental impedance data during the realization of the computations and the non-existence of time-domain impedance boundary conditions in ANSYS CFX 11 it was decided to apply a partially reflective boundary condition to capture the acoustic behavior of the downstream termination. The boundary condition used in this work can be classified as a formulation of acoustic non-reflective characteristic boundary conditions [39–41]. The non-reflective boundary condition formulation used in this case, in contrast to the method described by Poinsot and Lele [40], was derived for pressure based solvers [39]. The theoretical reflection factor $r(\omega)$ of the boundary condition formulation is a function of the relaxation coefficient $K = \sigma(1 - Ma^2)c/L$ [42],

$$r(\omega) = \frac{1}{\sqrt{1 + \left(\frac{2\omega}{K}\right)^2}}, \tag{6}$$

where σ denotes the coupling parameter, Ma the Mach number of the mean flow, c the sound speed, and L the domain size. By adjusting the coupling parameter σ the reflection factor $r(\omega)$ at the boundary condition can be modified and thus a fully reflective, a partially reflective or a non-reflective boundary condition can be realized. For the inclusion of the non-reflective boundary condition formulation, a DLR-CFX software extension implemented in ANSYS CFX 11 developed at the DLR-Institute of Combustion Technology, Stuttgart was applied [39].

At the inlet of the computational domain a classical fully reflective mass flow inlet boundary condition was applied. A constant mass flow of $\dot{m} = 42\,\mathrm{kg/h}$ with a temperature of $T = 300\,\mathrm{K}$ was set. The side planes of the computational domain were modeled by symmetry boundary conditions. This simplification can be justified because of a negligible swirling velocity component. The walls of the EWG were modeled with no-slip wall boundary conditions.

A three-dimensional compressible URANS approach was applied and turbulence was considered applying the standard k–ε model. This can be justified by the only slight impact of turbulence in the case considered here since according to preliminary numerically investigations the dissipation and dispersion of the entropy mode is very low. In addition, the influence of the turbulence on the propagation of the entropy noise downstream the nozzle is negligible. The spatial discretization was performed using the "high-order resolution scheme", which is essentially second-order accurate and bounded. A second-order backward Euler transient scheme was applied for the time discretization. Transient simulations were performed with a time step size of $50\,\mu\mathrm{s}$. The application of this time step size implies a cut-off frequency of $f = 400\,\mathrm{Hz}$ when considering a resolution of 50 sampling points per period (PPP) as sufficient.

The energy was induced to the system at the four cell layers of the computational grid that correspond to the location of the heating wires of the experimental setup. The energy transferred from the wires to the air flow depends on the wire temperature. So in accordance to measurements, Fig. 3 the energy supply inserted to the air flow was modeled assuming a linear increase and an exponential decrease of the energy source. The source term in the energy equation is implemented using a CFX User Fortran routine.

At the same positions where the microphones are located in the experimental setup, Section 2.1 the pressure fluctuations were monitored in the numerical simulation. In a first step a Reynolds averaged Navier–Stokes (RANS)

simulation was carried out to achieve a steady flow field solution of the EWG. Then, based on the steady simulation results, a subsequent URANS calculation was performed to simulate the time-dependent source of heat, the convection of the induced entropy mode and the generation and propagation of the entropy noise.

3.2. Acoustic sources of entropy noise

Dowling [43] derived the following inhomogeneous wave equation with source terms that are due to thermoacoustics:

$$\begin{aligned}\frac{1}{c_0^2}\frac{\partial^2 p}{\partial t^2}-\nabla^2 p = &-\frac{\partial}{\partial t}\left(\frac{\alpha\varrho_0}{c_p\varrho}\left(\sum_{n=1}^{N}\frac{\partial h}{\partial Y_n}\bigg|_{\varrho,p,Y_m}\varrho\frac{DY_n}{Dt}+\nabla\cdot q-\frac{\partial u_i}{\partial x_i}\tau_{ij}\right)\right)\\ &+\frac{\partial^2}{\partial x_i\partial x_j}(\varrho u_i u_j-\tau_{ij})\\ &+\frac{1}{c_0^2}\frac{\partial}{\partial t}\left(\left(1-\frac{\varrho_0 c_0^2}{\varrho c^2}\right)\frac{Dp}{Dt}-\frac{(p-p_0)}{\varrho}\frac{D\varrho}{Dt}\right)\\ &+\frac{\partial^2}{\partial x_i\partial t}(u_i\varrho_e).\end{aligned} \tag{7}$$

The "excess density" ϱ_e is defined as

$$\varrho_e=\varrho-\varrho_0-\frac{p-p_0}{c_0^2}, \tag{8}$$

where the suffix 0 denotes a suited reference value and $D/DT=\partial/\partial t+u_i\cdot\nabla$ the substantial time derivative. The right-hand side source terms of Eq. (7) describe all thermoacoustic sources. The first term represents the acoustic source due to irreversible flow processes. Lighthill's jet noise is considered in the second term. The third term implies acoustic sources generated by flow unsteadiness with varying mean density and sound speed from the ambient fluid. The last term is the one that describes the generation of acoustic waves by the change of momentum due to density inhomogeneities. This entropy noise source term is of dipole character in contrast to the direct combustion noise source terms which are monopole sources.

3.3. Results

3.3.1. Reference test case I

The Mach number distribution and the temperature distribution in the convergent–divergent nozzle achieved by the RANS simulation are displayed in Fig. 11. The air is supplied at the inlet and flows through the tube section upstream the nozzle, which contains the heating module with an average axial velocity of $u=12.4\,\mathrm{m/s}$ and a temperature of $T=300\,\mathrm{K}$. Downstream the heating module the air flow is accelerated in the convergent–divergent nozzle to a maximal Mach number of $Ma=1.32$. Due to the high acceleration of the air flow in the nozzle the temperature is decreasing to $T=222\,\mathrm{K}$. Subsequently, the air flow decelerates in the downstream tube section. The acceleration leads to a low pressure area within the nozzle.

In the following, all displayed and discussed acoustic pressure fluctuations correspond to the microphone located at $x_{AGR4}=1256\,\mathrm{mm}$.

In this work, a partially reflective boundary condition was applied to model the acoustic behavior of the downstream geometry. The use of the partially reflective boundary condition assumes a constant reflection factor and the phase shift is neglected. The adjustment of the coupling parameter σ in the boundary condition formulation results in the realization of a certain reflection factor $r(\omega)$ according to Eq. (6). In the present work the coupling parameter σ was adjusted in a way that the calculated pressure response showed close accordance to the measured one. Fig. 12a shows simulated pressure fluctuations applying a coupling parameter of $\sigma=1.8$. The superposition of downstream and reflected upstream propagating pressure waves results in pressure fluctuations that are in close agreement with the measurements. Both computed energy containing pressure signals indicate accordance in the shape as well as in the amplitude to the measurements. Only the oscillations after the two pressure signals show minor discrepancies. Numerical simulations

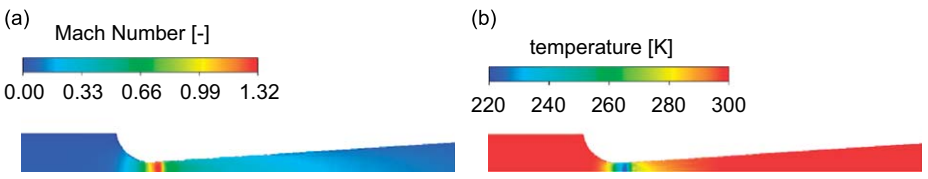

Fig. 11. Mach number and temperature distribution of the steady flow field. (a) Mach number; (b) temperature.

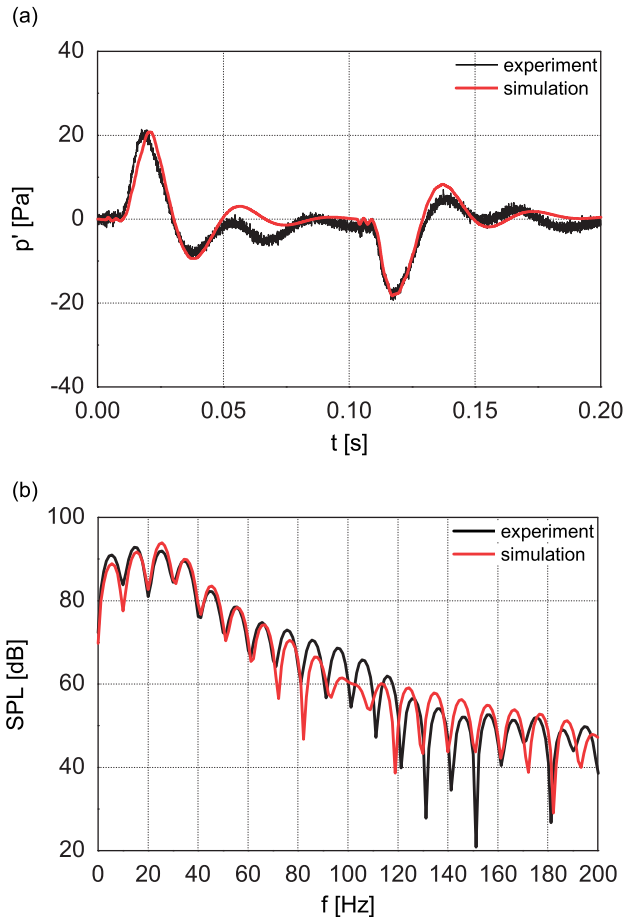

Fig. 12. Pressure fluctuation and pressure spectrum simulated with the partially reflective outlet boundary condition in comparison to measurements. (a) Pressure fluctuation; (b) pressure spectra.

applying fully reflective as well as non-reflective outlet boundary conditions, which were both not capable to reproduce the experimental data were presented and discussed in [44].

Fig. 12b shows the pressure spectra of the simulated pressure fluctuations and the experimental data obtained by a discrete fourier transform (DFT). Since the computed signal length of $\Delta t = 0.2$ s is too short to achieve a adequate frequency resolution in the low frequency range, the signal was extended by zero padding to the same length of the measured signal of $\Delta t = 0.9$ s. The pressure spectrum of the microphone measurement shows a majority of energy containing waves in the frequency range below $f = 100$ Hz. The observed spectrum for the simulated pressure response confirms this experimental observations. The simulated pressure spectrum displayed in Fig. 12b applying the partially reflective boundary condition is in very good agreement with the spectrum of the measured pressure fluctuations. Both spectra depict identical dominant frequencies. Additionally, the pressure amplitudes of the dominant frequencies are almost identical.

The remaining minor discrepancies between simulation and measurement are probably due to the modeling of the impedance of the downstream termination applying a partially reflective boundary condition. Acoustic waves interacting with the downstream geometry are reflected with a certain reflection factor and phase shift, both functions of the frequency. In the present work the application of the partially reflective boundary condition neglects the phase shift. Furthermore, there is a small numerically induced phase shift. Thus, the exact acoustic behavior at the boundary could only be captured by the application of proper time-domain CFD impedance boundary conditions that consider the measured reflection factor and the phase shift, both functions of the frequency [38,45].

3.3.2. *Mach number variation*

The performance of the applied numerical approach is further demonstrated by simulating different operating points of the EWG. Here, the inlet mass flow was varied to investigate the influence of the mean flow Mach number on the generated entropy noise. The supplied energy source was adjusted to keep the temperature increase constant and equal to $\Delta T = 9$ K. All simulations were carried out applying the partially reflective outlet boundary condition with a coupling parameter of $\sigma = 1.8$.

Fig. 13 shows the measured and calculated entropy noise in terms of the maximal pressure fluctuation as a function of the Mach number in the nozzle throat. The maximum in the pressure fluctuations of the experimental data increases up to a nozzle Mach number of $Ma \approx 0.7$ and then slightly decreases for higher nozzle Mach numbers. The numerical results are in very good agreement and within the precision of the measurements. They describe the same behavior, namely the increase up to nozzle Mach number of $Ma \approx 0.7$ and the subsequent decrease for higher nozzle Mach numbers. This behavior was not fully understood until now [46].

Additional numerical simulation were carried out, which evidence that the decline of the generated entropy noise for higher nozzle Mach numbers is not due to reflections which superimpose the pressure fluctuations. Therefore, at the end of the computational domain a non-reflective boundary condition was applied. To avoid reflections at the transition to the plenum upstream of the heating module the plenum was truncated and the inlet was modeled applying a non-reflective boundary condition. The results of the computations show also a decline of generated entropy noise for higher nozzle Mach numbers, Fig. 14.

To find an explanation for the decline of the generated entropy noise for higher nozzle Mach numbers, Fig. 13, numerical simulations of the EWG were conducted and the transient acoustic sources of entropy noise were determined. Thus, the source term q

$$q = \frac{\partial^2}{\partial x_i \partial t}(u_i \varrho_e) \tag{9}$$

of the inhomogeneous wave equation, Eq. (7) describing the acoustics generated by the acceleration of density inhomogeneities was computed and analyzed. It is to note here that the following analysis of the acoustic sources does not include all the intrinsic entropy noise sources of the applied CFD. Nevertheless, the purpose of the present simplified analysis is to find an explanation for the decline of the generated entropy noise for higher Mach numbers.

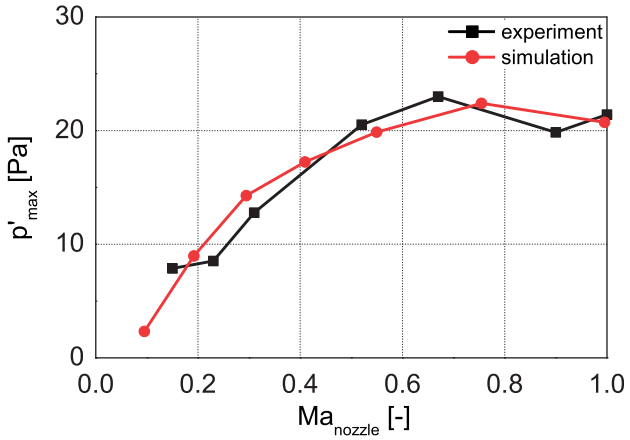

Fig. 13. Maximal pressure fluctuation over the nozzle Mach number.

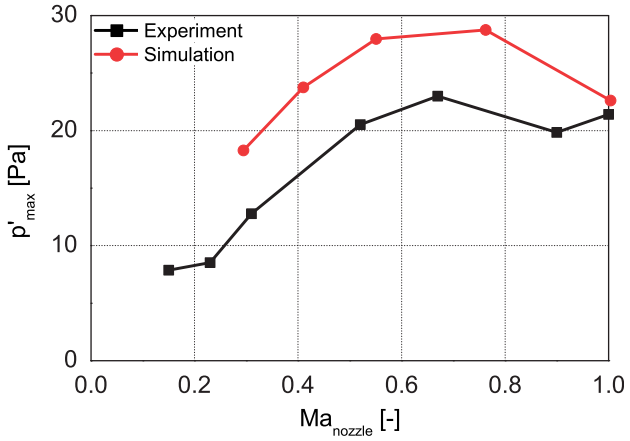

Fig. 14. Maximal pressure fluctuation over the nozzle Mach number computed with non-reflective boundary conditions.

Fig. 15. Nozzle domain for volume integration.

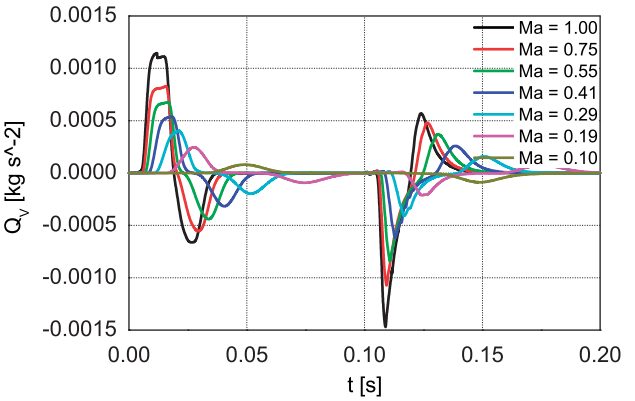

Fig. 16. Volume integral of the acoustic source over the convergent–divergent nozzle domain.

In order to investigate the strength of the acoustic sources the volume integral Q_V of the scalar acoustic source term q, Eq. (9) over the convergent–divergent nozzle domain V_N was computed

$$Q_V = \int_{V_N} q \, \mathrm{d}V. \tag{10}$$

A cutout of the computational domain with the nozzle domain highlighted is displayed in Fig. 15.

The volume integral as a function of time was calculated for the same flow conditions as for the computations with varying Mach number discussed above and is displayed in Fig. 16. The graphs indicate an increase of the strength of the acoustic source with increasing nozzle Mach number. This result shows that the decline of the generated entropy noise for higher nozzle Mach numbers is not caused by the strength of the acoustic source.

Besides the strength of the acoustic sources the transient computations provide the spacial distribution of the acoustic sources in the acceleration area. Fig. 17 illustrates representative instantaneous distributions of the acoustic sources of entropy noise for varying nozzle Mach number. Here, qualitative distributions of the timely varying acoustic sources at the moment of the strongest source intensity are shown. For the illustration of the acoustic source distributions different scales are used.

For all subsonic simulations the acoustic sources have a similar distribution. The acoustic sources are located in the convergent and partly in the divergent part of the nozzle. Positive acoustic sources are located nearby the axis and negative acoustic sources close to the wall. Furthermore, the area including positive sources is moving slightly downstream with increasing nozzle Mach number. In contrast to the subsonic configurations the source distribution for a nozzle Mach number of 1.0 is significantly different. The acoustic sources are mainly located in the divergent part of the nozzle. Positive acoustic sources are located upstream of the shock location, Fig. 11. Negative acoustic sources are located downstream of the shock position.

In the high Mach number configuration positive and negative acoustic sources generate positive and negative pressure fluctuations that propagate downstream and superimpose. Due to this superposition an attenuation of the acoustic waves occurs. This effect due to the acoustic source distribution in the high Mach number flow configurations causes the decline of the maximal pressure fluctuation for high nozzle Mach numbers, Fig. 13.

4. Numerical simulation: computational aeroacoustics (CAA)

In this section, a method to describe the propagation of perturbations from a flame in the combustion system is applied to the EWG experiment. This computational aeroacoustics method has originally been developed to describe the propagation of fan tone noise in an aero-engine inlet [47]. However, it will be shown, that the CAA method is able to model the indirect noise generation in a combustion system with some extensions to mathematical model and numerical method. The description of the model experiment is then eased by the available impedance model and the low resolution requirements of the method. Furthermore, another method for the identification of acoustic sources from the numerical

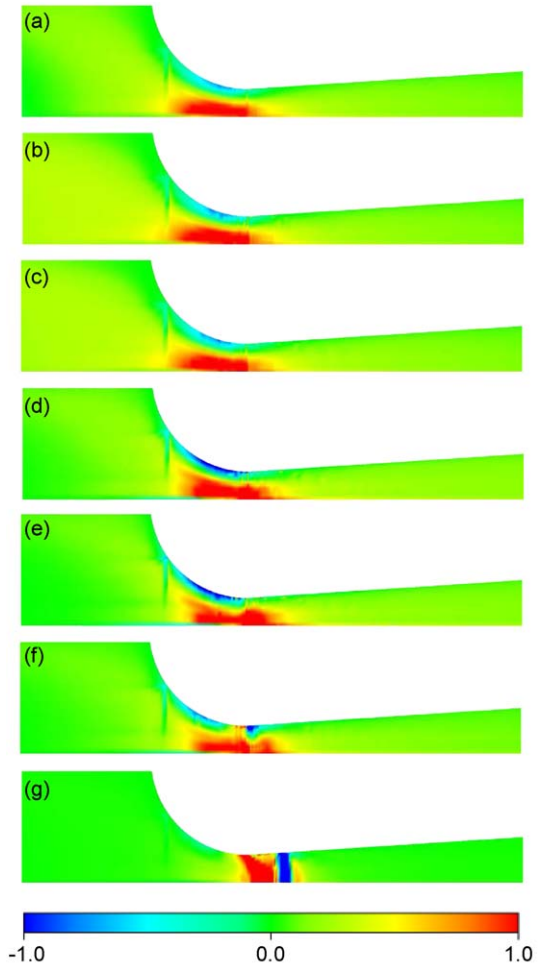

Fig. 17. Instantaneous acoustic source distribution for varying nozzle Mach number. The scaling is normalized with the respective maximum acoustic source. (a) $Ma_{\text{nozzle}} = 0.10$; (b) $Ma_{\text{nozzle}} = 0.19$; (c) $Ma_{\text{nozzle}} = 0.29$; (d) $Ma_{\text{nozzle}} = 0.41$; (e) $Ma_{\text{nozzle}} = 0.55$; (f) $Ma_{\text{nozzle}} = 0.75$; (g) $Ma_{\text{nozzle}} = 1.00$.

result, which is based on the acoustic intensity, is analysed with the EWG experiment. The acoustic intensity is also used to validate the current numerical result based on a conservation of the acoustic energy.

4.1. Mathematical model

The CAA method, which is described here, is intended to be the propagation part of a zonal approach as it is applied for fan tone problems. The mathematical model, which is described in more detail in this section, is based on a perturbation approach over a steady base flow. In addition, it is assumed in the following that the propagation of perturbations and the generation of indirect combustion noise can be described as small perturbation from an average flow state. Furthermore, perturbation sources and base flow are assumed to be known in advance, e.g. from a simulation using the method described in Section 3. However, a LES or DNS could serve as numerical method for the source zone as well. An overview on the general procedure of applying CAA methods for the simulation of indirect combustion noise can be found in Schemel et al. [48] and Richter and Thiele [49].

4.1.1. A perturbation approach to indirect combustion noise

To capture indirect combustion noise, the propagation of the hydrodynamic modes of perturbation, namely the vorticity and entropy mode in the definition of Chu and Kovasznay [1] has to be addressed by the perturbation approach as well. The mathematical model is a general formulation of the linearized Euler equations. A non-isentropic base flow and non-isentropic perturbations are assumed. Furthermore, the system is extended by an external source term describing a volumetric heat input. The resulting system is then applicable to the propagation of hydrodynamic and acoustic perturbations and additionally describes their interaction in a variable compressible mean flow regime. The governing

equations are given as follows (comp. [48]):

$$\frac{\mathrm{D}\varrho'}{\mathrm{D}t} + \mathbf{u}' \cdot \boldsymbol{\nabla}\varrho_0 + \varrho_0 \boldsymbol{\nabla} \cdot \mathbf{u}' + \varrho' \boldsymbol{\nabla} \cdot \mathbf{u}_0 = 0, \tag{11}$$

$$\frac{\mathrm{D}\mathbf{u}'}{\mathrm{D}t} + \frac{\varrho'}{\varrho_0}\mathbf{u}_0 \cdot \boldsymbol{\nabla}\mathbf{u}_0 + \mathbf{u}' \cdot \boldsymbol{\nabla}\mathbf{u}_0 + \frac{1}{\varrho_0}\boldsymbol{\nabla}p' = 0, \tag{12}$$

$$\frac{\mathrm{D}p'}{\mathrm{D}t} + \gamma p_0 \boldsymbol{\nabla} \cdot \mathbf{u}' + \mathbf{u}' \cdot \boldsymbol{\nabla}p_0 + \gamma p' \boldsymbol{\nabla} \cdot \mathbf{u}_0 = [\gamma - 1]\dot{q}. \tag{13}$$

The capital $\mathrm{D}/\mathrm{D}t$ denotes the material derivative with the mean flow as transport velocity:

$$\frac{\mathrm{D}\cdot}{\mathrm{D}t} = \frac{\partial\cdot}{\partial t} + \mathbf{u}_0 \cdot \boldsymbol{\nabla}\cdot \tag{14}$$

The above equations are linearized over an arbitrary mean flow, which can be obtained as solution of the nonlinear Euler equations, as it is done here. A steady CFD simulation of the combustion system can also serve as base flow. Taking advantage of the axial symmetry of the test set-up and flow conditions, the efficiency of the numerical method is improved by a two-dimensional axisymmetric approach [47]. The problem is formulated in a cylindrical coordinate system. The boundary conditions, flow field and perturbed flow field are assumed to be constant in the azimuthal direction. Similar to the modal axisymmetric approach for fan tone problems [47], this assumption allows to reduce the dimension of the problem by one.

4.2. Numerical method

In this section, the optimized numerical CAA method is described, which is applied to efficiently describe the propagation of perturbations at the low flow speed in the combustion chamber. The numerical high-order finite difference schemes can be applied as published. However, to avoid grid oscillations, filtering approaches have to be added for the current problem. These oscillations would usually pollute the solution for such high-order schemes, when they are applied to non-uniform strongly varying flow conditions. Furthermore, non-reflective and partially reflective boundary conditions in the time domain are described.

4.2.1. Discretization using the DRP scheme and a LDDRK time stepping

As the indirect noise generation involves the transport of perturbations over relatively long distances (in terms of the typical length scale of the perturbation), a high-order CAA scheme with low dissipation and dispersion properties [50,51] is chosen. Especially the hydrodynamic perturbations, for which the flow velocity defines the wave length, have to be correctly resolved to cover the indirect noise generation. Due to the large axial wavenumber of these perturbations in the audible frequency range, the resolution requirements to the spatial discretization are highly demanding.

4.2.2. Filtering algorithms

A 10th-order spatial low-pass filtering is applied here to avoid grid oscillations. In this combination, the current method allows to model the transport of perturbations down to about seven grid points per wavelength. Classical first- or second-order CFD methods would require about 50 PPW to obtain a similar dissipation error. Furthermore, the dispersion error of these low-order schemes cannot be removed for the typical backward stencils. When applied to combustion noise problems, the time-domain approach can exhibit its full potential. Transitional and broadband problems are much more efficiently addressed than with a frequency domain approach. Even nonlinear problems can be covered with only small increase in the modeling effort and the computational time [52] by simply adding the second-order interaction terms of the perturbations in Eqs. (11)–(13).

4.2.3. Acoustic boundary conditions

A radiation boundary condition [53] is used as fully anechoic termination. This boundary condition is modified by replacing the unit vector of the radiation direction by the unit normal vector of the radiating boundary, for the description of the in duct radiation problem. The modification is the exact acoustic boundary condition for frequencies below the cut-off frequency of the first higher mode. Above, a good approximation is given as long as the higher modes are far from cut-off. The fully and partially reflecting wall boundary conditions are based on a ghost point concept of Tam and Dong [54]. Details about the impedance boundary condition which is based on this hard wall boundary condition are given in the following section. At the axis a modal symmetrical boundary condition according to Li et al. [55] is applied.

4.2.4. Impedance model as replacement for connected systems

In this section the modeling of connected ducts and volumes by their impedance in a time-domain simulation is discussed. Usually these connected duct and turbo-machinery systems are not covered by the computational mesh for the simulation of the combustion system. Especially for combustion noise, reflections from up- and downstream duct ends are

an essential part of the acoustic solution. The extended Helmholtz resonator (EHR) [56] is used to model the reflections from a plenum with internal installations. Extending a model originally proposed by Ko [57] the generalized high frequency response of the impedance of a Helmholtz resonator with internal damping is given according to Rienstra [56] as

$$Z(\mathrm{i}\omega) = R + \mathrm{i}\omega m - \mathrm{i}\beta \cot(\tfrac{1}{2}\omega T_l - \mathrm{i}\tfrac{1}{2}\varepsilon). \tag{15}$$

The EHR, which is available in the current CAA method [58,59], is used to model a partly reflecting inflow in the plenum of the EWG experiment. The base flow is assumed to pass normal through the impedance surfaces. Thus, no model for the shear layer on the impedance surface (e.g. the boundary condition of Myers [60]) can be applied, and an effective impedance under the specific flow conditions has to be considered.

4.2.5. Mean flow field

Finally, the average flow state (denoted by the subscript $_0$) is an required prerequisite to simulate the propagation of small perturbations. The mean flow is varied in the same range as it is considered in the experiment. The mean flow fields used here are in general calculated using the CAAmethod on the mesh used for the perturbation approach later. A nonlinear Euler model, which is available in the CAAmethod [52] is applied and the boundary conditions excite a steady flow field. The boundary conditions at the in- and outflow are defined for all flow variables according to the compressible potential theory. A sponge layer is placed at the in- and outflow in order to remove reflections. To improve the convergence speed, a tree point stencil filter of second order is used for the mean flow calculation all over the domain. With this filter the CFL number could be increased up to 1. The system takes a steady state after 50 000 iterations. A mean flow field based on a three-dimensional steady compressible Reynolds averaged Navier–Stokes simulation of the nozzle is considered for comparison. The average flow field is interpolated by a second-order interpolation from the RANS mesh to the CAA mesh in this case. Furthermore, the mean flow field is filtered to remove short wave components in the mean flow field, which are not supported by the mesh.

4.3. Analysis of the results based on the acoustic intensity

4.3.1. Source location

The average acoustic source strength of a process in general follows from a time average balance of the acoustic energy:

$$\left\langle \frac{\partial e_a}{\partial t} \right\rangle_t + \boldsymbol{\nabla} \cdot \langle \mathbf{I}_a \rangle_t = \langle q_s \rangle_t. \tag{16}$$

Under the assumption of a statistically stationary solution for the process, the average change rate of the specific acoustic energy e_a is zero. Therefore, the divergence of the time averaged acoustic intensity is found to be equal to the average radiating acoustic source strength [61]:

$$\nabla \cdot \langle \mathbf{I}_a \rangle_t = \langle q_s \rangle_t. \tag{17}$$

Thus, based on Eq. (17) the average production of acoustic energy, which is considered as the source strength, can be calculated from the time averaged intensity.

4.3.2. Intensity definitions

The definition of the acoustic intensity is, however, not unique. The definition of Morfey [62] states the up to now most general expressions for acoustic intensity and energy:

$$e_a = \frac{p'^2}{2\varrho_0 c_0^2} + \frac{\varrho_0}{2}\mathbf{u}'_a \cdot \mathbf{u}'_a + \frac{p'}{\gamma p_0}\varrho_0 \mathbf{u}_0 \cdot \mathbf{u}'_a, \tag{18a}$$

$$\mathbf{I}_a = (p' + \varrho_0 \mathbf{u}_0 \cdot \mathbf{u}'_a)\left(\mathbf{u}'_a + \frac{p'}{\gamma p_0}\mathbf{u}_0\right). \tag{18b}$$

A conservation law applies in a potential flow field with this definition. This limitation theoretically means a purely potential mean flow with purely acoustic perturbation on top of it. However, in practice due to the negligible high-order interaction of the hydrodynamic and acoustic modes in a constant flow shown by Chu and Kovasznay [1], the conservation of the acoustic energy can be extended to such perturbations in a constant flow field. For other flow conditions, e.g. an entropy mode wave in any non-constant flow field, acoustic sources $\langle q_s \rangle_t \neq 0$ are present.

A generalized perturbation energy and the related energy flux was given by Myers [60]:

$$e_a = \frac{p'^2}{2\varrho_0 c_0^2} + \frac{\varrho_0}{2}\mathbf{u}'_a \cdot \mathbf{u}'_a + \varrho' \mathbf{u}_0 \cdot \mathbf{u}'_a, \tag{19a}$$

$$\mathbf{I}_a = (p' + \varrho_0 \mathbf{u}_0 \cdot \mathbf{u}'_a)\left(\mathbf{u}'_a + \frac{\varrho'}{\varrho_0}\mathbf{u}_0\right). \tag{19b}$$

This definition is also investigated here. A common problem of both definitions is the acoustic velocity perturbation $\mathbf{u}'_a$. The acoustic velocity perturbation is not available, as the velocity perturbation $\mathbf{u}'$ found in the CAA solution is a superposition of acoustic $\mathbf{u}'_a = \nabla\phi$ and vortical $\mathbf{u}'_\omega = \nabla \times \psi$ velocity perturbation in general. As long as $\mathbf{u}'_\omega$ remains small or the vortical perturbation is not correlated to p' or $\mathbf{u}'_a$, $\mathbf{u}'_a$ could be identified by $\mathbf{u}'$ of a numerical solution.

For indirect combustion noise, the initial entropy perturbation triggers both, acoustic and vortical perturbations, when passing a gradient of the base flow. Thus, the three modes of perturbation are connected and correlations can be found in each axial position. The relative phase of the secondary acoustic and vortical waves, which are triggered by an initial entropy perturbation, is fixed in case of indirect combustion noise. Thus, using the whole velocity perturbation $\mathbf{u}'$ instead of the acoustic velocity $\mathbf{u}'_a$ the intensity due to the vortical perturbation can be non-zero in time average.

To overcome the problem, a splitting of the velocity perturbation into acoustic and remaining velocity perturbation is required. However, to identify acoustic sources, $\langle \nabla \cdot \mathbf{I}_a \rangle_t$ is sufficient. The divergence of the acoustic intensity can be approximated based on the full velocity perturbation and the above intensity definition as follows:

$$\begin{aligned}
\nabla \cdot \mathbf{I}_a &= \nabla \cdot \left\{ p'\mathbf{u}'_a + \varrho_0 \mathbf{u}_0 \cdot \mathbf{u}'_a \mathbf{u}'_a + p'^2 \frac{1}{\gamma p_0}\mathbf{u}_0 + \mathbf{u}_0 \cdot \mathbf{u}'_a p' \frac{\mathbf{u}_0}{c_0} \right\} \\
&\approx (\nabla p') \cdot \mathbf{u}' + p' \nabla \cdot u' + \mathbf{u}' \cdot (\nabla \varrho_0)(\mathbf{u}_0 \cdot \mathbf{u}') + \varrho_0 \mathbf{u}' \cdot (\nabla \mathbf{u}_0) \cdot \mathbf{u}' \\
&\quad + \varrho(\mathbf{u}_0 \cdot \mathbf{u}')(\nabla \cdot \mathbf{u}') + \varrho(\mathbf{u}_0 \cdot \mathbf{u}')(\nabla \cdot \mathbf{u}') \\
&\quad + \frac{2p'}{\gamma p_0}(\nabla p') \cdot \mathbf{u}_0 - p'^2 \frac{\nabla p_0 \cdot \mathbf{u}_0}{\gamma p_0^2} + \frac{p'^2}{\gamma p_0} \nabla \cdot \mathbf{u}_0 \\
&\quad + \frac{p'}{c_0}\mathbf{u}_0 \cdot \mathbf{u}' \nabla \cdot \mathbf{u}_0 + p' \nabla \cdot \mathbf{u}' \mathbf{u}_0 \cdot \frac{\mathbf{u}_0}{c_0} + \frac{1}{c_0}(\nabla p' \cdot \mathbf{u}')(\mathbf{u}_0 \cdot \mathbf{u}_0) \\
&\quad + \frac{p'}{c_0}\mathbf{u}' \cdot (\nabla \mathbf{u}_0) \cdot \mathbf{u}_0 - p'(\mathbf{u}_0 \cdot \mathbf{u}') \frac{\mathbf{u}_0 \cdot \nabla c_0}{c_0^2},
\end{aligned} \tag{20}$$

where the rotational component of mean flow and acoustic perturbation velocity are assumed to be zero such that the second vector form can be used to replace

$$\begin{aligned}
\nabla(\mathbf{u}_0 \cdot \mathbf{u}') &= \mathbf{u}_0 \cdot \nabla \mathbf{u}' + \mathbf{u}' \cdot \nabla \mathbf{u}_0 + u_0 \times (\nabla \times \mathbf{u}') + u_0 \times (\nabla \times \mathbf{u}') \\
&\approx \mathbf{u}_0 \cdot \nabla \mathbf{u}' + \mathbf{u}' \cdot \nabla \mathbf{u}_0.
\end{aligned}$$

The same approximation can be applied for $\nabla(\mathbf{u}' \cdot \mathbf{u}')$. The local average speed of sound is defined as $c^2 = \gamma p_0 \varrho_0^{-1}$. Furthermore, shear velocity terms are assumed to be zero for the more or less planar acoustic perturbation in the current investigation.

4.3.3. Introduction of the source power level (QPL)-scale

The unit of the source strength is $\mathrm{W/m^3}$ like for a specific acoustic power. To obtain the acoustic power, which is input in average, the source strength is related to a reference volume. Here $V_{\mathrm{ref}} \approx 10^{-5}\,\mathrm{m^3}$ is used. For a better visualization with a large dynamic range of the acoustic source strength, a logarithmic scale is chosen, which is based on the sound power level (SPL). The absolute value of the source power is considered, to obtain equal logarithmic levels for the generation and annihilation of acoustic energy. For a compact overview, the scales are put together cutting values below a predefined threshold off and adding the original sign of P_{in} afterwards. Accordingly the acoustic source power level QPL is defined as

$$\mathrm{QPL} = \mathrm{sgn}(\mathrm{P}_{in}) 10 \log_{10}\left[\max\left(\frac{|\mathrm{P}_{in}|}{10^{-12}\,\mathrm{W}}, 1\right)\right]. \tag{21}$$

The QPL becomes zero, if the absolute value of the input source power is below the threshold of $10^{-12}\,\mathrm{W}$.

Comparison of the intensity definitions. The different definitions of the energy flux are studied with a simple generic flow duct excited by a harmonic entropy source. The flow Mach number based on a nonlinear Euler solution with slip wall assumption ranges between $Ma = 0.17$ and 0.51 in the wide and narrow duct sections, respectively. Acoustic sources are expected to be observed in the acceleration zones of the flow, only. The generalized perturbation energy should not be generated or annihilated at all.

The results of the preliminary investigation are summarized in Fig. 18. The color plots in the upper part of each subfigure shown the QPL. As can be seen from Fig. 18(a), if the general definition of a perturbation energy of Myers [60] is applied, the QPL locates sources all over the duct, which is not the expected result. Rather the general perturbation energy should locate no sources for the boundary value problem, which just converts energy from the entropy mode to the acoustic mode. The original definition of the acoustic intensity by Morfey [62] results in a better identification of acoustic sources, as the pressure perturbation is not effected by the entropy mode as it was the case before. Thus, the results shown in Fig. 18(b) show no artificial sources in the inlet duct. However, there are also artificial sources inside the straight duct section between nozzle and diffuser and in the straight outlet duct. As a splitting of acoustic and vortical velocity field is not yet available, the overall velocity perturbation is applied, which leads to the observed error. A splitting technique for the velocity perturbation field into acoustic and vortical perturbation is highly desired in the future. The modified calculation of the source strength of Eq. (20) finally improves the solution in the outlet duct as can be seen from Fig. 18(c).

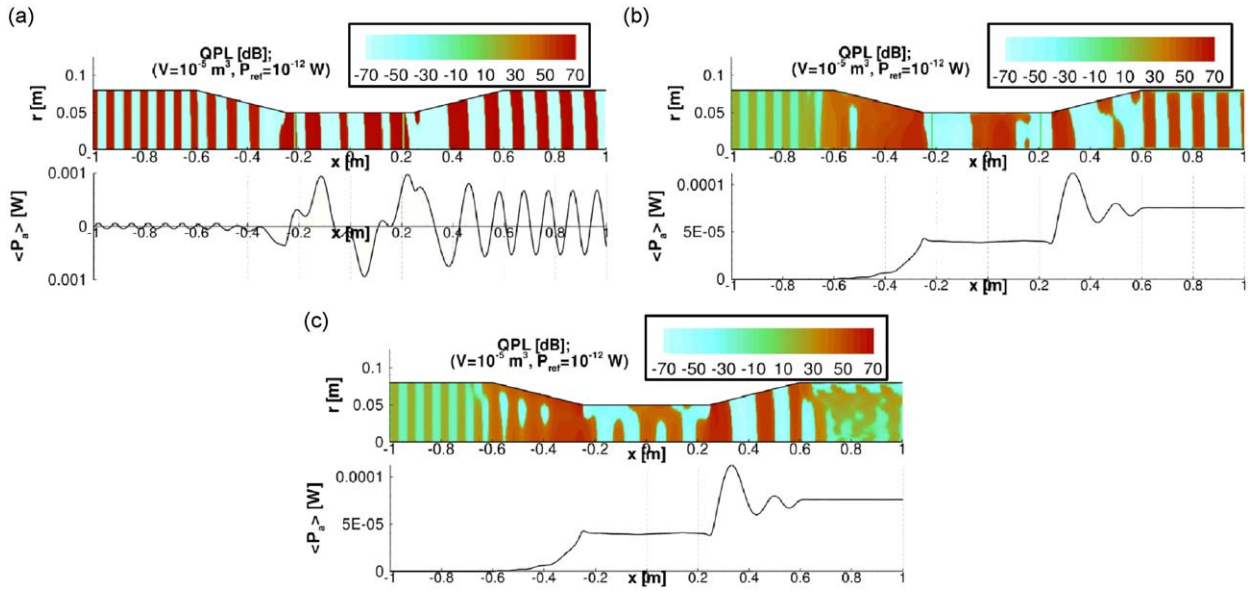

Fig. 18. QPL based on different definitions of the acoustic intensity and the divergence. (a) Energy flux definition of Myers, Eqs. (15)–(17) [60], $\mathbf{u}_1$ replaced by $\mathbf{u}'$ (Eq. (19b)); (b) acoustic intensity definition of Morfey [62], $\mathbf{u}'_a$ replaced by $\mathbf{u}'$, Eq. (18b); (c) calculation of the divergence according to Eq. (20).

The source strength in the straight inlet and outlet duct sections is more than one order below the ones in the nozzle and diffuser. However, the narrow duct with higher flow velocities is still polluted by the remaining terms describing the correlation between acoustic and vortical perturbation.

4.3.4. Solution validation based on the global conservation of acoustic energy

To prove a numerical result, the time averaged acoustic intensity component with an orientation parallel to the axis is integrated over a disc closing the duct section at a given axial position x. The resulting average acoustic energy flux P_a through this disc is given as

$$\langle P_a(x)\rangle_t = \int_{S_{\mathrm{disc}}(x)} \langle I_{a,x}(x)\rangle_t \, \mathrm{d}S. \tag{22}$$

The acoustic energy flux must be constant and is a measure of the quality of the numerical solution in the absence of sources. Where physical sources are present, the acoustic power flux denotes the overall production of acoustic power in an axial position.

Examples for the evaluation of the acoustic power are given in Fig. 18 in the lower part of each figure. The perturbation energy of Myers [60] produces unexpected axial variations all over the duct (Fig. 18(a)). The modified definition of Morfey [62] produces a nearly constant energy flux in the straight duct sections (Figs. 18(b) and (c)). Small variations in the ducts downstream the first contraction are probably due to the missing distinction of vortical and acoustic velocity component. The contraction and dilatation of the duct show variations, which are attributed to the indirect noise generation. The wavelength of the initial harmonic entropy perturbation in the numerical experiment is much smaller than the nozzle contraction and diffuser dilation. Thus, multiple positive and negative sources are found in these regions and the acoustic intensity varies with the position.

4.4. CAA results

In this section the CAA-results from the simulations of the EWG experiment are summarized. First an overview about the normalized peak pressure response to a heating pulse is given in Section 4.4.1. In this step the whole settling chamber volume was included in the simulation as shown in Fig. 19. However, different from the CFD simulation, the baffle plate and the inflow are not resolved; rather the whole lower wall of the plenum is considered as inflow, hard wall or partially reflective wall, respectively, denoted as Z_{in} in Fig. 19. In a second step, the resolved settling chamber is replaced by a time-domain impedance boundary condition in the inflow plane of the heated duct section as can be seen in Fig. 19 as Z_{Plenum}, which results in a reduced computational domain for the CAA simulation. An approximation of the plenum impedance based on an identification with the parameters of a low frequency Helmholtz resonator is considered in Section 4.4.2. Finally, a source location and results validation based on the acoustic intensity is carried out with the result in Section 4.4.3.

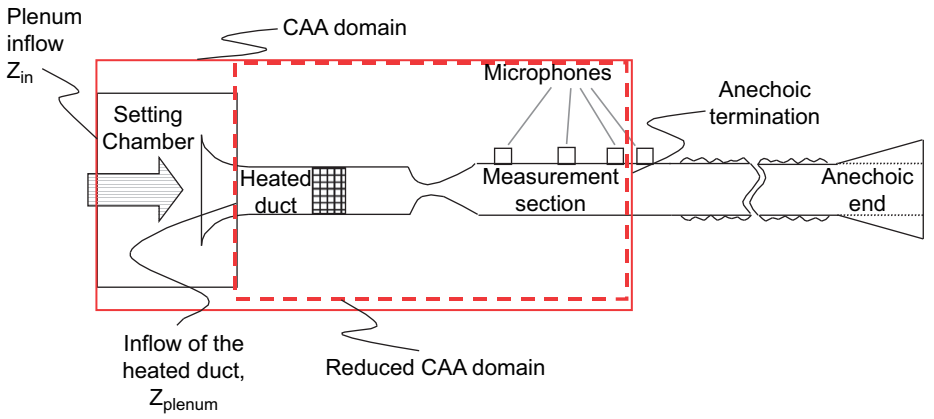

Fig. 19. Sketch of the EWG with the computational domains for the CAA simulation and the relevant boundary conditions.

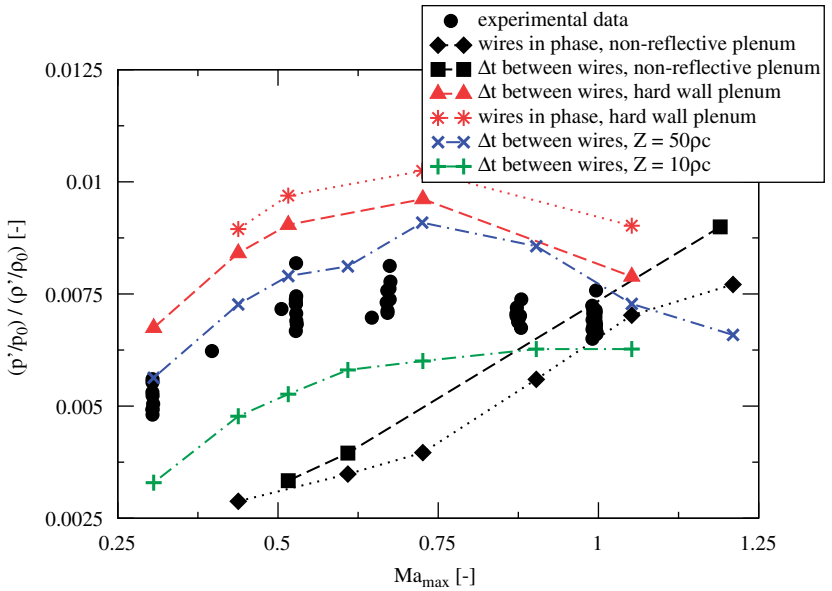

Fig. 20. Normalized transmission coefficient between entropy perturbation in the inlet duct and maximum pressure perturbation in the outlet duct.

4.4.1. Peak pressure signal in the outlet duct in response to a heating pulse

First, a variation of the maximum nozzle Mach number with respect to the mass flow rate in the flow duct is carried out following the experiment. All results of the parameter variations are summarized in Fig. 20. The perturbation variables are non-dimensionalized by the related flow variables. The pressure perturbation is normalized by the pressure in the outlet duct, and the non-isentropic density perturbation is normalized by the mean density in the heated duct section. The abscissa of Fig. 20 shows a Mach number, which is defined by the maximum flow velocity in the unperturbed state normalized by the local speed of sound.

First of all it is observed from Fig. 20, that a fully non-reflective modeling of the plenum (square and diamond) produces a large deviation from the experimentally observed peak pressure response over the nozzle Mach number. The plenum reflection, either with a fully reflective plenum (stars and triangles) or partially reflective plenum by an approximately purely real impedance (x and plus) leads to a much better reproduction of the trend in the experimental data for the peak pressure response.[1] In the CFD simulations of Section 3, the plenum reflection is included due to the constant mass flow condition at the inlet and the correctly resolved meshing of the exact baffle plate and inflow geometry. In the CAA

[1] The experimental data are based on the corrected Mach number in the nozzle throat, which reaches maximally $Ma = 1$. Therefore, the supersonic cases are all mapped to $Ma = 1$ for the experiment, whereas the CAA simulation is related to the maximum Mach number, which can reach supersonic conditions. The subsonic flow conditions do not differ.

simulation the whole inflow is considered non-, partially or fully reflective, respectively. With any of the fully or partly reflective plenum inflow models a saturation of the peak pressure response is observed around $Ma = 0.7$. The peak pressure level of the anechoic and reflective plenum equalizes with the flow reaching transonic conditions in the nozzle. However, none of the inflow impedances considered here is able to reproduce the exact swing off frequency for $Ma = 0.7$.

Finally, it can be seen from Fig. 20 that the transmission coefficient of the system response shown in Fig. 20 is not independent of the shape and amplitude of the actual heat supply comparing the results denoted by square and diamond and the ones with triangles and stars, respectively. Two different pulse shapes for the heat input are considered. They are triggered by the same rectangular input. One considers the delayed heating of the wire modules, which leads to a much steeper raise and fall of the entropy perturbation than the heating in phase considered for the other case. Even though there are some quantitative differences for the two different heating pulses, the qualitative trends of the related cases varying with the heat input are similar, such that an approximation of the exact pulse shape could be applied.

4.4.2. Theoretically predicted plenum impedance

The CAA simulations indicate a strong dependency of the observed pressure response to the unknown impedance of the settling chamber Z_{Plenum} in Fig. 19. This impedance has not yet been measured. It can only approximately be calculated from a theoretical consideration of the geometry of the chamber. Especially the real part of the impedance of the plenum with flow remains subject to theoretical speculation or empirical measurement. The CFD simulation of Section 3 on the other hand shows that the impedance of the anechoic end is required to reproduce the result, when the settling chamber with the air supply up to the mass flow regulation is included into the simulation. On the other hand it was not possible to find a termination impedance with the EHR model for the anechoic termination of the outlet duct, which produces similar reflections like the partially reflective CFD boundary condition, which is described above. This may be due to an insufficiency of the EHR model. However, the description of the anechoic termination by the EHR could not be followed any further.

Therefore, the plenum impedance is estimated by the analogy of the low frequency limit of the EHR to the low frequency Helmholtz resonator in this section. The connection between the dimensions of the low frequency Helmholtz resonator and its impedance is well described, except for the resistance. However, for zero damping of the cavity fluid ($\varepsilon = 0$) and at the face sheet ($R = 0$), the remaining parameters of the EHR can be identified with the geometric parameters of a low frequency Helmholtz resonator as follows:

$$\frac{T_l}{2} = \frac{2\pi}{c}\sqrt{\frac{VL}{S_0}}, \tag{23a}$$

$$\beta = c\frac{S_0}{V}\frac{T_l}{2} \tag{23b}$$

and

$$m = \frac{L}{c}. \tag{23c}$$

The plenum geometry is given as cavity volume $V = 4.6\,\text{l}$ and open area of the neck $S_0 = 7.1\,\text{cm}^2$. The neck length L is difficult to calculate. The plenum has only a negligibly short neck to the duct. A length correction has to be used, as the plenum is directly connected to the computational domain. The usual empirical length correction for the waves moving inside the cavity is in the order of the neck radius, which would lead to $L = 1.5\,\text{cm}$, whereas the consideration of a length correction for cylindrical volumes by Alster [63] would result in $L = 0.2\,\text{cm}$. Depending on the length, the resonant frequency is obtained to be $f_0 \approx 44 \ldots 170\,\text{Hz}$. f_0 is the inverse of the halve response time T_l. Consequently, the non-dimensional model parameters are obtained to be $\beta \approx 0.3 \ldots 0.17$ and $m \approx 2 \times 10^{-5}$. The damping of the cavity volume due to the installations and the inflow is not clear. The same applies to the face sheet reactance, which is probably very small without flow, but increases with increasing flow velocity. The theoretical consideration gives an estimate for the parametric range and allows a better representation of the plenum by the EHR. The parameters for the EHR are chosen as follows in the simulation: $T_l = \frac{1}{270}\,\text{s}$, $\beta = 0.4$ and $m = \frac{1}{20\,000}$. The face sheet resistance is assumed to be small ($R = 0.5$) and a considerable cavity damping is obtained by setting $\text{e}^{-\varepsilon} = 0.8$.

The result obtained with this representation of the plenum closely approximates the pressure response, as can be seen from Fig. 21. However, there are still some differences in the detail. Furthermore, the choice of the EHR parameters influences the observed result. Therefore, the result cannot be seen as validation of the numerical method unless the correct plenum impedance is known from the experiment. In the following section, this impedance is used to provide the numerical data for the source location based on the acoustic intensity and validate the numerical solution.

4.4.3. Quality analysis and source location

Selected results of the intensity analysis are presented in Fig. 22. The partially reflecting plenum, which has been described in Section 4.4.2 is considered. The direct source effect of the heat input is visible with the QPL-scale in the region between $x = 0$ and $0.036\,\text{m}$. However, the acoustic energy input by the direct source ($\text{QPL} \approx 70\,\text{dB}$) is several orders of magnitude below the maximum observed energy input in the whole duct. The indirect source strength found in the nozzle

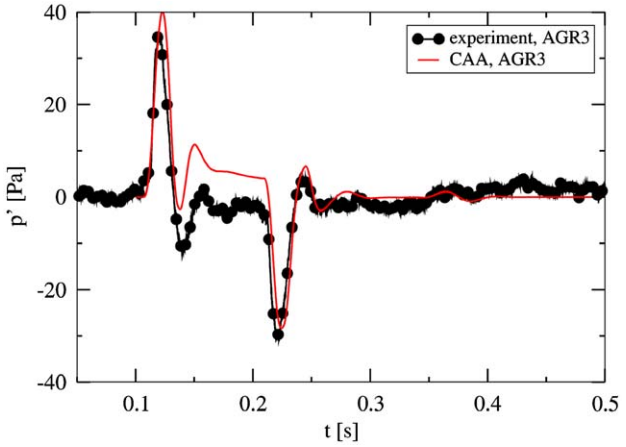

Fig. 21. Pressure response at the microphones in the exhaust duct for $Ma = 0.73$.

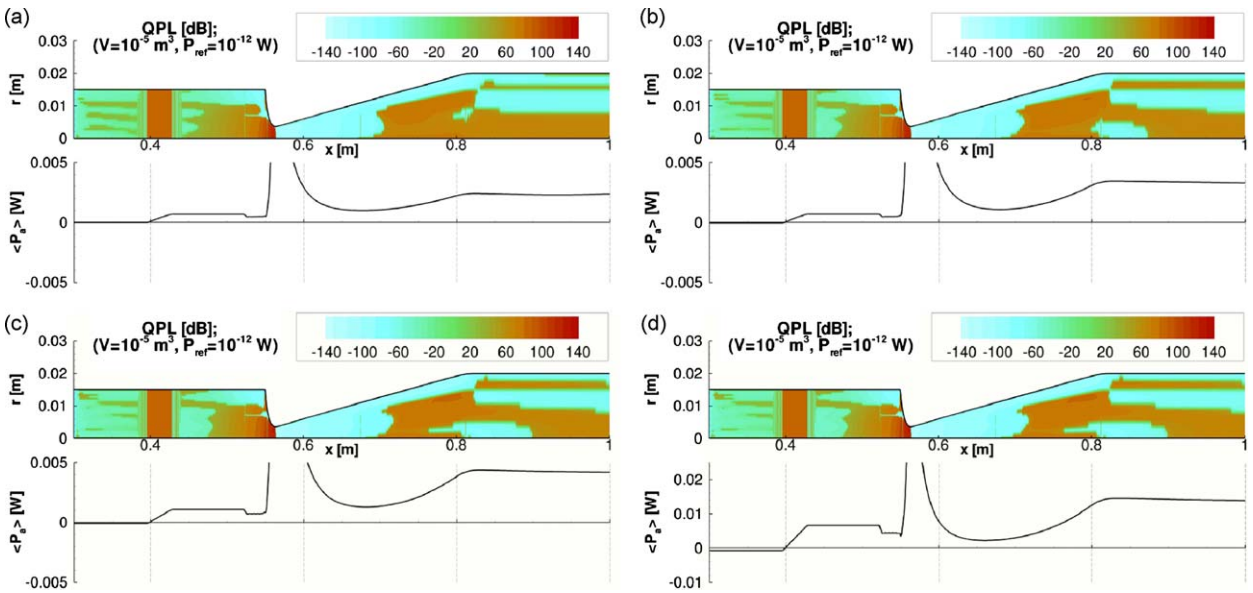

Fig. 22. Average acoustic source strength QPL (top as contour plot) and axial acoustic power flux P_a (below as lines). (a) $Ma = 0.31$; (b) $Ma = 0.52$; (c) $Ma = 0.73$; (d) $Ma = 1.05$.

and diffuser is much larger (QPL $\approx$ 120 dB). The most powerful acoustic sources are found in the nozzle throat. Due to the sinks fund in the diffuser, the sources in the nozzle radiate only a small fraction of the acoustic energy into the downstream duct section. Furthermore, the integral acoustic source strength depends on the size of the source volume. The direct source region forms an one order larger volume, than the strong sources in the nozzle. To obtain a direct comparison of these values, the source volume has to be considered with the interpretation, such that the sources in the nozzle must be leveled off by 10 dB to obtain the volume corrected source strength. Furthermore, the strong energy annihilation in the diffuser leads to an acoustic short circuit with the strong sources in the nozzle. Some additional acoustic sources are located further downstream in the diffuser. However, these sources may originate from the simplification of the acoustic velocity perturbation $\mathbf{u}'_a$ to the overall velocity perturbation. A strong, large vortex is generated by the entropy perturbation passing the inhomogeneous flow field in the nozzle. As described above, this vortex is correlated with the acoustic waves in the exhaust duct. Both originate from the passage of the initial entropy perturbation through the nozzle. Therefore, the vortical perturbation contributes to the modified intensity in time average.

Below the contour plots the overall acoustic power flux in time average $\langle P_a \rangle_t$ is given for each flow speed. While the color map is the same for all figures, the overall acoustic power shown below was adjusted to represent the observed levels better. The above observations are supported by $\langle P_a \rangle_t$. In the region of the heat module, the acoustic power increases almost linear and the acoustic power flux is negative upstream (left in Fig. 22) of the heating module and positive downstream of the module. The positive acoustic power in the inlet duct indicates that the direct sources dominate the effective flux of

acoustic energy here. The linear increase directly corresponds to the heated duct section, which was also identified as source region with the QPL. Furthermore, there is an approximately constant acoustic power in the straight duct section between heat module and nozzle. The small decrease and variation in front of the nozzle is due to an interpolation error for the two grid blocks involved in the integration there. There is an intense increase of the acoustic power flux in the nozzle then, which leads to large amplitudes of $\langle P_a \rangle_t$. For a better presentation the peak has been cut-off in Fig. 22. The intense right running acoustic waves originating from the nozzle are then annihilated in the diffuser directly following the nozzle throat. The field in the diffuser may include trapped waves, which initially run upstream and get reflected at the nozzle. The net transport of acoustic energy by these waves is zero over the whole pulse. The reflected waves may also be involved in the annihilation of acoustic energy in the diffuser. Altogether the acoustic power flux in the diffuser becomes very low and increases again to the outlet. The acoustic power flux in the outlet duct becomes constant again, even though there are remaining acoustic sources identified by the QPL in the outlet duct.

Taking the information of the QPL together with $\langle P_a \rangle_t$, the direct source mechanism is found to radiate with the full positive source strength, without any perturbation from negative sources into the heated inlet duct section. The sources in the nozzle have a different nature. Strong positive and negative sources are found with the QPL, which cancel in average. The resulting acoustic high power flux is localized to the throat between nozzle and diffuser. The acoustic power flux is then increased by the sources in the exit region of the diffuser again.

The acoustic intensity has been analysed for several different assumptions about the reflection coefficient of the plenum. It has been found that the plenum reflection does not qualitatively alter the findings of the QPL or the $\langle P_a \rangle_t$. This is in contrast to earlier investigations, which were using the modified definition of the power flux generated by an arbitrary perturbation of Myers [60], which has been shown to be unable to distinguish between acoustic and entropy perturbation. Furthermore, the Myers [60] formulation is not able to locate the acoustic sources in the heated duct region, which were clearly found now. However, the definition of the acoustic intensity may still be improved by a distinction of acoustic and other perturbations.

5. Conclusion

Research was performed on a dedicated test set up in order to investigate the entropy noise mechanism under clearly defined flow and boundary conditions.

In order to reduce the complexity of the generation of entropy noise at a combustor exit, a reference test rig with clearly defined boundary and flow conditions has been set up within this work. In this test rig well controlled entropy waves were generated by electrical heating. The noise emission of the entropy waves when passing a convergent/divergent nozzle was accurately measured. For comparison with numerical simulations two reference cases have been selected and documented in detail. In addition to this a parametric study on the quantities affecting entropy noise was conducted.

CFD simulations of the generation and propagation of entropy noise were conducted applying a three-dimensional compressible URANS approach. Here, in comparison to hybrid CFD/CAA approaches the acoustics are directly resolved by the CFD computation. The impedance of the flow geometry downstream the outlet boundary condition was modeled applying a partially reflective boundary condition, assuming a constant reflection coefficient. Computed time resolved pressure fluctuations and pressure spectrum are in very good agreement with the measurements. Simulations of the maximum sound pressure level for different operating points with varying nozzle Mach number agree very well with experimental data, too.

The EWG experiment has also been considered numerically with a CAA method. First a large parameter variation has been carried out to investigate the transfer function between initial entropy perturbation and peak pressure response in the measurement section of the outlet duct. It is found that the method in combination with an impedance boundary condition modeling reflections from the plenum and especially from the inflow of the plenum is able to reproduce the experimental observation. Different impedance models for the plenum have been considered in the CAA simulation. Using a theoretical estimate for the impedance of the inflow, the swing off of the pressure in the outlet duct can be recovered with a very good approximation of the experimental result.

Both the impedance of the plenum and the outflow impedance are able to reproduce the experimental observation and there are evidences that reflections from both sides are also present in the experiment. The current results clearly indicate the importance of reflections from up- and downstream system components for the combustion acoustics in such a system. The indirect and direct noise is superimposed with these reflections and the sound field in the whole test set up essentially depends on the reflections. As technical combustion systems use similar large plenum volumes with internal installations for swirl stabilized flames, the result is probably transferable to these systems.

A source location for the distinction of direct and indirect combustion noise has been carried out with the numerical data. The CFD simulation was analyzed using the source term from an acoustic analogy. The CAA result is analyzed based on the acoustic energy and intensity. Even though the methods are quite different, both methods are able to locate the sources of indirect combustion noise.

The source term of the acoustic analogy in the CFD simulation indicates that the source strength of the indirect noise increases with the maximum flow Mach number in the nozzle. However, the declined peak pressure response for Mach numbers above $Ma = 0.7$ can be explained by the instantaneous contribution of acoustic source terms with opposite sign at

the highest source level. The simultaneous positive and negative contributions of the source term are only found for higher Mach numbers and cause the decline of the peak pressure.

Such a temporal resolved monitoring of the acoustic sources is not possible with the acoustic intensity, which was used for the source location in the CAA result. However, the acoustic energy based source location gives an overview about the noise generation over the whole pulse. The time averaged source strength locates a similar structure with a source in the nozzle and a sink in the following diffuser section for all flow conditions considered here. These sources are found to be orders of magnitude larger than the direct sources from the heating.

Both source location methods are able to identify strong indirect sources in the throat of the nozzle. Both methods shown an increasing source strength with the Mach number. The indirect sources are found to be several orders of magnitude larger than the direct source due to the heating. A main fraction of the indirect sources seems to cancel in average in the current configuration. A single nozzle or diffuser could probably produce much higher amplitudes, which underlines the importance of the combustion chamber exit nozzle for the indirect noise generation. However, the peak pressure response seems not to be effected by the canceling sources up to $Ma = 0.7$. In addition to the reflections, the timing of the sources is an important factor for the resulting peak pressure response. Both parameters could act as mediator for noise reduction measures in combustion systems.

In summary the presented results enable a deep understanding of the entropy noise phenomenon especially due to the combination of experiments and two fairly different numerical approaches. However, even in spite of the simplified model case the investigated entropy noise mechanism still appears in a comprehensive complexity. Therefore, and because of the increasing relevance as an aero-engine noise source, further research on entropy noise, also under application of the presented reference cases, should be performed.

Acknowledgments

The authors gratefully acknowledge the financial support by the German Research Foundation (DFG) within the framework of the research unit FOR 486 "Combustion Noise". We also want to thank Prof. Ulf Michel for his impulse to this entropy noise research and all the subsequent fruitful discussions. The authors want to acknowledge Dr. Klaus Ehrenfried for the many discussions about the understanding of acoustic sources and source location methods which finally lead to the acoustic intensity based source location method.

References

[1] B.-T. Chu, L.S.G. Kovasznay, Non-linear interactions in a viscous heat-conducting compressible gas, *Journal of Fluid Mechanics* 3 (1958) 494–514 (Part 5).
[2] C.L. Morfey, Amplification of aerodynamic noise by convected flow inhomogeneities, *Journal of Sound and Vibration* 31 (4) (1973) 391–397.
[3] M.J. Lighthill, On sound generated aerodynamically, *Proceedings of the Royal Society London A* (211) (1952) 564–587.
[4] M.S. Howe, Contributions to the theory of aerodynamic sound, with application to excess jet noise and the theory of the flute, *Journal of Fluid Mechanics* 71 (1975) 625–673 (Part 4).
[5] J.E. Ffowcs Williams, M.S. Howe, The generation of sound by density inhomogeneities in low Mach number nozzle flows, *Journal of Fluid Mechanics* 70 (1975) 605–622 (Part 3).
[6] H.Y. Lu, An analytical model for entropy noise of subsonic nozzle flow, *AIAA 4th Aeroacoustic Conference*, 77-1366, AIAA, 1977.
[7] F.E. Marble, S.M. Candel, Acoustic disturbances from gas non-uniformities convected through a nozzle, *Journal of Sound and Vibration* 55 (2) (1977) 225–243.
[8] N.A. Cumpsty, F.E. Marble, Core noise from gas turbine exhausts, *Journal of Sound and Vibration* 54 (2) (1977) 297–309.
[9] N.A. Cumpsty, F.E. Marble, The interaction of entropy fluctuations with turbine blade rows; a mechanism of turbojet engine noise, *Proceedings of the Royal Society London A* (357) (1977) 323–344.
[10] N.A. Cumpsty, Jet engine combustion noise: pressure, entropy and vorticity perturbations produced by unsteady combustion or heat addition, *Journal of Sound and Vibration* 66 (4) (1979) 527–544.
[11] W.C. Strahle, Combustion noise, *Progress in Energy and Combustion Science* 4 (3) (1978) 157–176.
[12] D.C. Mathews, N.F. Rekos Jr., R.T. Nagel, Combustion noise investigations, Technical Report FAA RD-77-3, Pratt & Whitney Aircraft Group, United Technologies Corporation, East Hartford, Connecticut, USA, 1977.
[13] A.W. Bloy, The pressure waves produced by the convection of temperature disturbances in high subsonic nozzle flows, *Journal of Fluid Mechanics* 94 (1979) 465–475 (Part 3).
[14] W.C. Strahle, M. Muthukrishnan, Correlation of combustor rig sound power data and theoretical basis of results, *AIAA Journal* 18 (3) (1980) 269–274 (article no. 79-0587R).
[15] M. Tanahashi, S. Tsukinari, T. Saitoh, T. Miyauchi, G. Choi, M. Ikame, T. Kishi, K. Harumi, K. Hiraoka, On the sound generation and its controls in turbulent combustion field, *in proceedings 3rd Symposium on Smart Control of Turbulence*, March 2002, Tokyo, Japan, 2001.
[16] E.E. Zukoski, J.M. Auerbach, Experiments concerning the response of supersonic nozzles to fluctuating inlet conditions, *Journal of Engineering for Power* (75-GT-40) (1976) 60–63 (ASME).
[17] M.S. Bohn, Noise Produced by the Interaction of Acoustic Waves and Entropy Waves with High-speed Nozzle Flows, PhD Thesis, California Institute of Technology, Pasadena, California, USA, 1976.
[18] M.S. Bohn, Response of a subsonic nozzle to acoustic and entropy disturbances, *Journal of Sound and Vibration* 52 (2) (1977) 283–297.
[19] M. Muthukrishnan, W.C. Strahle, D.H. Neale, Separation of hydrodynamic, entropy, and combustion noise in a gas turbine combustor, *AIAA Journal* 16 (4) (1978) 320–327.
[20] A. Guedel, A. Farrando, Experimental study of turboshaft engine core noise, *Journal of Aircraft* 23 (10) (1986) 763–767.
[21] M.M. Martinez, Determination of combustor noise from a modern regional aircraft turbofan engine, *12th AIAA/CEAS Aeroacoustics Conference*, 2006-2676, Cambridge, MA, 2006.
[22] M. Harper-Bourne, A. Moore, H. Siller, A study of large aero-engine combustor noise, *14th AIAA/CEAS Aeroacoustics Conference*, 2008-2942, Vancouver, Canada, 2008.

[23] J.J. Keller, W. Egli, J. Hellat, Thermally induced low-frequency oscillations, *Journal of Applied Mathematics and Physics (ZAMP)* 36 (1985) 250–274.
[24] J.J. Keller, Thermoacoustic oscillations in combustion chambers of gas turbines, *AIAA Journal* 33 (12) (1995) 2280–2287.
[25] A.P. Dowling, Acoustics of unstable flows, in: T. Tatsumi, E. Watanabe, T. Kambe (Eds.), *Theoretical and Applied Mechanics*, Elsevier, Amsterdam, 1996.
[26] A.P. Dowling, Combustion noise and active control, *VKI Lecture*, VKI, 1997.
[27] A.P. Dowling, S. Hubbard, Instability in lean premixed combustors, *Proceedings of the Institution of Mechanical Engineers*, vol. 214, Part A, IMechE, 2000.
[28] W. Polifke, C.O. Paschereit, K. Döbbeling, Constructive and destructive interference of acoustic and entropy waves in a premixed combustor with a choked exit, *The International Journal of Acoustics and Vibration* 6 (3) (2001) 135–146.
[29] T. Sattelmayer, Influence of the combustor aerodynamics on combustion instabilities from equivalence ratio fluctuations, *ASME Turbo Expo 2000*, 2000-GT-0082, ASME, Munich, Germany, 2000.
[30] G. Ali, J.K. Hunter, The resonant interaction of sound waves with a large amplitude entropy wave, *SIAM Journal on Applied Mathematics* 61 (1) (2000) 131–148.
[31] A.P. Dowling, The calculation of thermoacoustic oscillations, *Journal of Sound and Vibration* 180 (4) (1995) 557–581.
[32] M. Zhu, A.P. Dowling, K.N.C. Bray, Self excited oscillations in combustors with spray atomisers, *ASME Turbo Expo 2000*, 2000-GT-108, ASME, Munich, Germany, 2000.
[33] J. Eckstein, E. Freitag, C. Hirsch, T. Sattelmayer, Experimental study on the role of entropy waves in low-frequency oscillations for a diffusion burner, *ASME Turbo Expo 2004*, GT2004-54163, ASME, Vienna, Austria, 2004.
[34] J. Eckstein, On the Mechanisms of Combustion Driven Low-Frequency Oscillations in Aero-Engines, Dr.-Ing. Dissertation, Technische Universität München, München, Germany, 2004.
[35] M. Leyko, F. Nicoud, T. Poinsot, Comparison of indirect and direct combustion noise in aircraft engines, *11th CEAS-ASC Workshop and 2nd Scientific Workshop of X3-Noise: Experimental and Numerical Analysis and Prediction of Combustion Noise*, Instituto Superior Tecnico, Lisbon, Portugal, 2007.
[36] L. Enghardt, Y. Zhang, W. Neise, Experimental verification of a radial mode analysis technique using wall-flush mounted sensors, *137th Meeting of the Acoustical Society of America*, Berlin, 1999, pp. 15–19.
[37] R. Maier, J. Zillmann, A. Roure, M. Winninger, L. Enghardt, U. Tapken, W. Neise, H. Antoine, E. Bouty, Active control of fan tone noise from aircraft engines, *7th AIAA/CEAS Aeroacoustics Conference*, 2001-2220, Maastricht, 2001.
[38] A. Widenhorn, B. Noll, M. Aigner, impedance boundary conditions for the numerical simulation of gas turbine combustion systems, *ASME Turbo Expo*, GT2008-50445, Berlin, Germany, 2008.
[39] A. Widenhorn, B. Noll, M. Aigner, Accurate boundary conditions for the numerical simulation of thermoacoustic phenomena in gas-turbine combustion chambers, *ASME Turbo Expo 2006*, GT2006-90441, ASME, Barcelona, Spain, 2006.
[40] T. Poinsot, S. Lele, Boundary conditions for direct simulations of compressible viscous flows, *Journal of Computational Physics* (101) (1992) 104–129.
[41] M. Baum, T. Poinsot, D. Thevenin, Accurate boundary conditions for multicomponent reactive flows, *Journal of Computational Physics* (116) (1994) 247–261.
[42] L. Selle, F. Nicoud, T. Poinsot, Actual impedance of nonreflecting boundary conditions: implications for computation of resonators, *AIAA Journal* 42 (5) (2004) 958–964.
[43] A. Dowling, Thermoacoustics and Instabilities, in: D.G. Crighton et al. (ed.) Modern Methods in Analytical Acoustics, Springer, Berlin.
[44] B. Mühlbauer, A. Widenhorn, M. Liu, B. Noll, M. Aigner, Fundamental mechanism of entropy noise in aero-engines: numerical simulation, *ASME Turbo Expo 2007*, GT2007-27173, ASME, Montreal, Canada, 2007.
[45] A. Huber, W. Polifke, Impact of fuel supply impedance on combustion stability of gas turbines, *ASME Turbo Expo*, GT2008-51193, Berlin, Germany, 2008.
[46] F. Bake, N. Kings, I. Röhle, Fundamental mechanism of entropy noise in aero-engines: experimental investigation, *Journal of Engineering for Gas Turbines and Power* 130 (1) (2008) 011202-1–011202-6.
[47] X. Li, C. Schemel, U. Michel, F. Thiele, On the azimuthal mode propagation in axisymmetric duct flows, AIAA Paper 2002-2521, 2002.
[48] C. Schemel, F. Thiele, F. Bake, B. Lehmann, U. Michel, Sound generation in the outlet section of gas turbine combustion chambers, *10th AIAA/CEAS Aeroacoustics Conference*, 2004-2929, Manchester, UK, 2004.
[49] C. Richter, F. Thiele, CAA Tools for the simulation of indirect combustion noise from transonic nozzle flows, *11th CEAS-ASC Workshop, Experimental and Numerical Analysis and Prediction of Combustion Noise*, CEAS-ASC, Lisbon, Portugal, paper 15, 2007.
[50] C.K.W. Tam, C. Webb, Dispersion-relation-preserving finite difference schemes for computational aeroacoustics, *Journal of Computational Physics* 107 (2) (1993) 262–281.
[51] F.Q. Hu, M.Y. Hussaini, J.L. Manthey, Low-dissipation and low-dispersion Runge–Kutta schemes for computational acoustics, *Journal of Computational Physics* 124 (1) (1996) 177–191.
[52] C. Richter, L. Panek, F. Thiele, On the application of CAA-methods for the simulation of indirect combustion noise, AIAA Paper 2005-2919, 2005.
[53] C. Bogey, C. Bailly, Three-dimensional non-reflective boundary conditions for acoustic simulations: far field formulation and validation test cases, *Acta Acustica United with Acoustica* 88 (2002) 462–471.
[54] C.K.W. Tam, Z. Dong, Wall boundary conditions for high-order finite difference schemes in computational aeroacoustics, *Theoretical and Computational Fluid Dynamics* 6 (6) (1994) 303–322.
[55] X. Li, C. Schemel, U. Michel, F. Thiele, Azimuthal sound mode propagation in axisymmetric flow ducts, *AIAA Journal* 42 (10) (2004) 2019–2027.
[56] S.W. Rienstra, Impedance models in time domain, including the extended Helmholtz resonator model, AIAA Paper 2006-2686, 2006.
[57] S.-H. Ko, Sound attenuation in lined rectangular ducts and its application to the reduction of aircraft engine noise, *Journal of the Acoustic Society of America* 50 (6, Part 1) (1971) 1418–1432.
[58] X.D. Li, C. Richter, F. Thiele, Time-domain impedance boundary conditions for subsonic mean flow, *Journal of Acoustical Society of America* 119 (5) (2006) 2665–2676.
[59] C. Richter, F. Thiele, X.D. Li, M. Zhuang, Comparison of time-domain impedance boundary conditions for lined duct flows, *AIAA Journal* 45 (6) (2007) 1333–1345.
[60] M.K. Myers, On the acoustic boundary condition in the presence of flow, *Journal of Sound and Vibration* 71 (8) (1980) 429–434.
[61] C. Richter, F. Thiele, The stability of time explicit impedance models, AIAA Paper 2007-3538, 2007.
[62] C. Morfey, Acoustic energy in non-uniform flows, *Journal of Sound Vibration* 14 (2) (1971) 159–170.
[63] M. Alster, Improved calculation of resonant frequencies of Helmholtz resonators, *Journal of Sound and Vibration* 24 (1) (1972) 63–85.